primers: mPlxnB1 forward, 5′-CAGATGTCTGGTGCCACATC-3′; mPlxnB1 reverse, 5′-CCCTCACACCACACACAGTC-3′; PlxnB2 forward, 5′-AGGGGAGCCTCTCTACAAGC-3′; PlxnB2 reverse, 5′-TCGATCC-CTTCATCCTGAAC-3′; mMet forward, 5′-GTTGGTCCCGCGAT-GAGT-3′; mMet reverse, 5′-GAGTGAGTAAGGTGCCTCCAG-3′; mCCL17 forward, 5′-AGTGGAGTGTTCCAGGGATG-3′; mCCL17 reverse, 5′-CTGGTCACAGGCCGTTTTAT-3′; mMSR1 forward, 5′-CTG-GACAAACTGGTCCACCT-3′; mMSR1 reverse, 5′-CCCCTTCTC-TCCCTTTTGTC-3′; mHGF forward, 5′-AGGAACAGGGGCTTTAC-GTT-3′; mHGF reverse, 5′-GTCAAATTCATGGCCAAACC-3′; mCD72 forward, 5′-CTGCACATCTCTGTCCTCCA-3′; mCD72 reverse, 5′-TCAGAGTCCTGCCTCCACTT-3′; mIL-10 forward, 5′-CCAAGCCT-TATCGGAAATGA-3′; mIL-10 reverse, 5′-TTTTCACAGGGGAGAA-ATCG-3′; mMSCF1 forward, 5′-GACCCTCGAGTCAACAGAGC-3′; mMSCF1 reverse, 5′-TGCTTCCTGGGTCAAAAATC-3′; bactin forward, 5′-TGTTACCAACTGGGACGACA-3′; and bactin reverse, 5′-GGGGT-GTTGAAGGTCTCAAA-3′.

Analysis of human monocytes

PMBCs were obtained and stained as previously described (50, 53). In brief, PMBCs were obtained from healthy blood donors by Ficoll density gradient centrifugation. Mononuclear cells were washed three times in PBS, and 25×10^6 cells were plated on 10-cm diameter Petri dishes. Nonadherent cells were removed after a 1-h incubation and examined (sample labeled as day 0). A portion of the PMBCs was kept in culture for 48 h in the absence of differentiating factors (sample labeled as day 2). Surface staining of cells was performed using the following antibodies: anti-Sema4D (Beckman Coulter) and anti-CD14 (monocyte-specific marker; Invitrogen). Isotype controls were performed in each experiment.

To evaluate the response of monocytes to different stimuli, PBMCs were purified by magnetic beads and stimulated for 24 h in the presence of one of the following molecules: 100 ng/ml IL-10, 100 ng/ml TGF-β, 100 ng/ml M-CSF (PrepoTech), 100 mg/ml LPS, or 100 nM PMA (Sigma-Aldrich). Hypoxia was induced by incubating cells in a 3% O_2 atmosphere. After 24 h, cells were washed with PBS and total mRNA was extracted using the TRIzol extraction kit. 1 µg RNA was retrotranscribed using M-MLV reverse transcriptase minus H in a final volume of 40 µl, according to manufacturer's protocol. cDNA was amplified using the following primers: hSema4D forward, 5′-CCAGCTCTTCCAGGACTTTG-3′; hSema4D reverse, 5′-ACTTTTATCCGGGCACACAG-3′; hTNFa forward, 5′-CCA-AGCCCTGGTATGAGC-3′; hTNFa reverse, 5′-GGGCAATGATCC-CAAAGTAG-3′; hIL-10 forward, 5′-GTTGCCAAGCCTTGTCTGA-3′; hIL-10 reverse, 5′-GGCCTTGCTCTTGTTTTCAC-3′; hGAPDH forward, 5′-ACAGTCAGCCGCATCTTCTT-3′; and hGAPDH reverse, 5′-GACAAGCTTCCCGTTCTCAG-3′.

Immunoblot analysis

WT or Sema4D TAMs were lysed with Laemmli buffer (67.5 mM Tris, 2% SDS), and 100 µg of proteins was run on 8% SDS-PAGE. TSA and MLP29 cells were lysed in EB buffer, as previously described (8). 500 µg of protein was immunoprecipitated with 2 µg anti–plexin B1 and 2 µg of rabbit anti–mouse Ig for 3 h in a rotating wheel at 4°C. 100 µg of protein and immunoprecipitations were subjected to 8% SDS-PAGE. Anti-Sema4D antibody was purchased from BD Biosciences; anti–β-actin (I-19) and anti–plexin B1 (A-8) were purchased from Santa Cruz Biotechnology, Inc.

Matrigel plugs

500 µl of Matrigel (Becton Dickinson) was injected subcutaneously in the ventral area of Sema4D KO mice. Matrigel plugs contained 2×10^5 TAMs (WT or Sema4D derived) in the presence or absence of 100 ng/ml anti–plexin B1 (ec6.9), anti-VSV antibodies, or 100 nM PHA-665752. Control plugs contained 36 ng/ml HGF (R&D Systems), 200 ng/ml b-FGF (R&D Systems), or an equivalent amount of PBS (negative control). Each experimental condition was analyzed in triplicate. 14 d after plug implantation, 5 min before death, mice received a 200-µl tail-vein injection containing 20 mg/ml dextran-FITC (Sigma-Aldrich). Plugs were collected, immediately fixed in formalin, and analyzed using a fluorescent microscope.

Sema4D silencing

TSA cells were transduced with MISSION shRNA lentiviral plasmid pLKO.1-puro (clone no. TRCN0000067495; Sigma-Aldrich) targeting the following sequence: 5′-CCACAGCTACACATCAGTCAT-3′. Cells were selected using 2 µg/ml puromycin.

Statistical analyses

For analyses of experimental data, comparisons of data were performed using the Student's *t* test. All p-values are two tailed. $P < 0.001$ was considered significant.

Online supplemental material

Fig. S1 shows that different syngeneic breast cancer cell lines grafted into Sema4D KO mice give rise to smaller tumors when compared with those observed in WT mice. Fig. S2 provides information regarding the expression of plexin B1 (high affinity receptor for Sema4D) in TSA cells; it also shows that Sema4D is able to promote the motogenic/invasive ability of the examined breast cancer cells. Fig. S3 illustrates that Sema4D produced by platelets does not contribute to tumor growth. Fig. S4 shows that human macrophages, but not monocytes, express Sema4D; it also shows that Sema4D expression is probably linked to macrophage activation better than differentiation. Fig. S5 confirms that macrophages obtained from Sema4D KO mice are functionally similar to those taken from WT mice. Fig. S6 shows that Sema4D silencing in mammary tumor cells does not affect tumor growth. Online supplemental material is available at http://www.jem.org/cgi/content/full/jem.20072602/DC1.

We are grateful to Dr. P. Gabriele and his staff for the irradiation of mice, to Dr. A. Sottile for the evaluation of platelet inhibition, to Drs. A. Elia and M. Mazzone for help in analyzing the human macrophages, and to all our colleagues that shared interesting and fruitful discussions with us. The excellent technical assistance of R. Albano, L. Palmas, M. Crudelini, and R. Lo Noce is gratefully acknowledged. J.R. Sierra was mainly responsible for the experimental work; S. Corso, V. Cepero, and P. Conrotto also helped perform experiments; L. Caione and W. Piacibello performed bone marrow transplants; A. Cignetti performed the Sema4D expression profile in human monocytes; and A. Kumanogoh and H. Kikutani provided Sema4D KO mice. All of the authors analyzed and discussed the data. S. Giordano and L. Tamagnone guided the project and contributed to the experimental design and to data interpretation.

This work was supported by Associazione Italiana per la Ricerca sul Cancro (AIRC) grants to S. Giordano and L. Tamagnone, and Regione Piemonte grants to S. Giordano, L. Tamagnone, and S. Corso. J.R. Sierra is a Consejo Nacional de Ciencia y Tecnología-Mexico fellow, and S. Corso is an AIRC fellow.

The authors have no conflicting financial interests.

Submitted: 10 December 2007
Accepted: 20 May 2008

REFERENCES

1. Pasterkamp, R.J., and A.L. Kolodkin. 2003. Semaphorin junction: making tracks toward neural connectivity. *Curr. Opin. Neurobiol.* 13:79–89.
2. Kolodkin, A.L., D.J. Matthes, and C.S. Goodman. 1993. The semaphorin genes encode a family of transmembrane and secreted growth cone guidance molecules. *Cell.* 75:1389–1399.
3. Tamagnone, L., S. Artigiani, H. Chen, Z. He, G.I. Ming, H. Song, A. Chedotal, M.L. Winberg, C.S. Goodman, M. Poo, et al. 1999. Plexins are a large family of receptors for transmembrane, secreted, and GPI-anchored semaphorins in vertebrates. *Cell.* 99:71–80.
4. Takegahara, N., H. Takamatsu, T. Toyofuku, T. Tsujimura, T. Okuno, K. Yukawa, M. Mizui, M. Yamamoto, D.V. Prasad, K. Suzuki, et al. 2006. Plexin-A1 and its interaction with DAP12 in immune responses and bone homeostasis. *Nat. Cell Biol.* 8:615–622.
5. Behar, O., J.A. Golden, H. Mashimo, F.J. Schoen, and M.C. Fishman. 1996. Semaphorin III is needed for normal patterning and growth of nerves, bones and heart. *Nature.* 383:525–528.

6. Kumanogoh, A., and H. Kikutani. 2001. The CD100-CD72 interaction: a novel mechanism of immune regulation. *Trends Immunol.* 22:670–676.
7. Bismuth, G., and L. Boumsell. 2002. Controlling the immune system through semaphorins. *Sci. STKE.* 2002:RE4.
8. Giordano, S., S. Corso, P. Conrotto, S. Artigiani, G. Gilestro, D. Barberis, L. Tamagnone, and P.M. Comoglio. 2002. The semaphorin 4D receptor controls invasive growth by coupling with Met. *Nat. Cell Biol.* 4:720–724.
9. Tse, C., R.H. Xiang, T. Bracht, and S.L. Naylor. 2002. Human Semaphorin 3B (SEMA3B) located at chromosome 3p21.3 suppresses tumor formation in an adenocarcinoma cell line. *Cancer Res.* 62:542–546.
10. Christensen, C.R., J. Klingelhofer, S. Tarabykina, E.F. Hulgaard, D. Kramerov, and E. Lukanidin. 1998. Transcription of a novel mouse semaphorin gene, M-semaH, correlates with the metastatic ability of mouse tumor cell lines. *Cancer Res.* 58:1238–1244.
11. Carmeliet, P., and M. Tessier-Lavigne. 2005. Common mechanisms of nerve and blood vessel wiring. *Nature.* 436:193–200.
12. Miao, H.Q., S. Soker, L. Feiner, J.L. Alonso, J.A. Raper, and M. Klagsbrun. 1999. Neuropilin-1 mediates collapsin-1/semaphorin III inhibition of endothelial cell motility: functional competition of collapsin-1 and vascular endothelial growth factor-165. *J. Cell Biol.* 146:233–242.
13. Conrotto, P., D. Valdembri, S. Corso, G. Serini, L. Tamagnone, P.M. Comoglio, F. Bussolino, and S. Giordano. 2005. Sema4D induces angiogenesis through Met recruitment by Plexin B1. *Blood.* 105:4321–4329.
14. Basile, J.R., T. Afkhami, and J.S. Gutkind. 2005. Semaphorin 4D/plexin-B1 induces endothelial cell migration through the activation of PYK2, Src, and the phosphatidylinositol 3-kinase-Akt pathway. *Mol. Cell. Biol.* 25:6889–6898.
15. Basile, J.R., A. Barac, T. Zhu, K.L. Guan, and J.S. Gutkind. 2004. Class IV semaphorins promote angiogenesis by stimulating Rho-initiated pathways through plexin-B. *Cancer Res.* 64:5212–5224.
16. Basile, J.R., R.M. Castilho, V.P. Williams, and J.S. Gutkind. 2006. Semaphorin 4D provides a link between axon guidance processes and tumor-induced angiogenesis. *Proc. Natl. Acad. Sci. USA.* 103:9017–9022.
17. Basile, J.R., K. Holmbeck, T.H. Bugge, and J.S. Gutkind. 2007. MT1-MMP controls tumor-induced angiogenesis through the release of semaphorin 4D. *J. Biol. Chem.* 282:6899–6905.
18. Hall, K.T., L. Boumsell, J.L. Schultze, V.A. Boussiotis, D.M. Dorfman, A.A. Cardoso, A. Bensussan, L.M. Nadler, and G.J. Freeman. 1996. Human CD100, a novel leukocyte semaphorin that promotes B-cell aggregation and differentiation. *Proc. Natl. Acad. Sci. USA.* 93:11780–11785.
19. Shi, W., A. Kumanogoh, C. Watanabe, J. Uchida, X. Wang, T. Yasui, K. Yukawa, M. Ikawa, M. Okabe, J.R. Parnes, et al. 2000. The class IV semaphorin CD100 plays nonredundant roles in the immune system: defective B and T cell activation in CD100-deficient mice. *Immunity.* 13:633–642.
20. Elhabazi, A., S. Delaire, A. Bensussan, L. Boumsell, and G. Bismuth. 2001. Biological activity of soluble CD100. I. The extracellular region of CD100 is released from the surface of T lymphocytes by regulated proteolysis. *J. Immunol.* 166:4341–4347.
21. Zhu, L., W. Bergmeier, J. Wu, H. Jiang, T.J. Stalker, M. Cieslak, R. Fan, L. Boumsell, A. Kumanogoh, H. Kikutani, et al. 2007. Regulated surface expression and shedding support a dual role for semaphorin 4D in platelet responses to vascular injury. *Proc. Natl. Acad. Sci. USA.* 104:1621–1626.
22. Masuda, K., T. Furuyama, M. Takahara, S. Fujioka, H. Kurinami, and S. Inagaki. 2004. Sema4D stimulates axonal outgrowth of embryonic DRG sensory neurones. *Genes Cells.* 9:821–829.
23. Kumanogoh, A., C. Watanabe, I. Lee, X. Wang, W. Shi, H. Araki, H. Hirata, K. Iwahori, J. Uchida, T. Yasui, et al. 2000. Identification of CD72 as a lymphocyte receptor for the class IV semaphorin CD100: a novel mechanism for regulating B cell signaling. *Immunity.* 13:621–631.
24. Winberg, M.L., J.N. Noordermeer, L. Tamagnone, P.M. Comoglio, M.K. Spriggs, M. Tessier-Lavigne, and C.S. Goodman. 1998. Plexin A is a neuronal semaphorin receptor that controls axon guidance. *Cell.* 95:903–916.
25. Trusolino, L., and P.M. Comoglio. 2002. Scatter-factor and semaphorin receptors: cell signalling for invasive growth. *Nat. Rev. Cancer.* 2:289–300.
26. Torisu, H., M. Ono, H. Kiryu, M. Furue, Y. Ohmoto, J. Nakayama, Y. Nishioka, S. Sone, and M. Kuwano. 2000. Macrophage infiltration correlates with tumor stage and angiogenesis in human malignant melanoma: possible involvement of TNFalpha and IL-1alpha. *Int. J. Cancer.* 85:182–188.
27. Welm, A.L., J.B. Sneddon, C. Taylor, D.S. Nuyten, M.J. van de Vijver, B.H. Hasegawa, and J.M. Bishop. 2007. The macrophage-stimulating protein pathway promotes metastasis in a mouse model for breast cancer and predicts poor prognosis in humans. *Proc. Natl. Acad. Sci. USA.* 104:7570–7575.
28. von Tell, D., A. Armulik, and C. Betsholtz. 2006. Pericytes and vascular stability. *Exp. Cell Res.* 312:623–629.
29. Yamagishi, S., and T. Imaizumi. 2005. Pericyte biology and diseases. *Int. J. Tissue React.* 27:125–135.
30. Ganss, R. 2006. Tumor stroma fosters neovascularization by recruitment of progenitor cells into the tumor bed. *J. Cell. Mol. Med.* 10:857–865.
31. Boccaccio, C., G. Sabatino, E. Medico, F. Girolami, A. Follenzi, G. Reato, A. Sottile, L. Naldini, and P.M. Comoglio. 2005. The MET oncogene drives a genetic programme linking cancer to haemostasis. *Nature.* 434:396–400.
32. Chiodoni, C., M. Iezzi, C. Guiducci, S. Sangaletti, I. Alessandrini, C. Ratti, F. Tiboni, P. Musiani, D.N. Granger, and M.P. Colombo. 2006. Triggering CD40 on endothelial cells contributes to tumor growth. *J. Exp. Med.* 203:2441–2450.
33. Albini, A., and M.B. Sporn. 2007. The tumour microenvironment as a target for chemoprevention. *Nat. Rev. Cancer.* 7:139–147.
34. Zalatnai, A. 2006. Molecular aspects of stromal-parenchymal interactions in malignant neoplasms. *Curr. Mol. Med.* 6:685–693.
35. Mantovani, A., T. Schioppa, C. Porta, P. Allavena, and A. Sica. 2006. Role of tumor-associated macrophages in tumor progression and invasion. *Cancer Metastasis Rev.* 25:315–322.
36. Lewis, C.E., and J.W. Pollard. 2006. Distinct role of macrophages in different tumor microenvironments. *Cancer Res.* 66:605–612.
37. Sica, A., A. Saccani, B. Bottazzi, N. Polentarutti, A. Vecchi, D.J. Van, and A. Mantovani. 2000. Autocrine production of IL-10 mediates defective IL-12 production and NF-kappa B activation in tumor-associated macrophages. *J. Immunol.* 164:762–767.
38. Barberis, D., S. Artigiani, A. Casazza, S. Corso, S. Giordano, C.A. Love, E.Y. Jones, P.M. Comoglio, and L. Tamagnone. 2004. Plexin signaling hampers integrin-based adhesion, leading to Rho-kinase independent cell rounding, and inhibiting lamellipodia extension and cell motility. *FASEB J.* 18:592–594.
39. Christensen, J.G., R. Schreck, J. Burrows, P. Kuruganti, E. Chan, P. Le, J. Chen, X. Wang, L. Ruslim, R. Blake, et al. 2003. A selective small molecule inhibitor of c-Met kinase inhibits c-Met-dependent phenotypes in vitro and exhibits cytoreductive antitumor activity in vivo. *Cancer Res.* 63:7345–7355.
40. Pollard, J.W. 2001. Tumour-stromal interactions. Transforming growth factor-beta isoforms and hepatocyte growth factor/scatter factor in mammary gland ductal morphogenesis. *Breast Cancer Res.* 3:230–237.
41. Balkwill, F., and A. Mantovani. 2001. Inflammation and cancer: back to Virchow? *Lancet.* 357:539–545.
42. Lin, E.Y., J.F. Li, L. Gnatovskiy, Y. Deng, L. Zhu, D.A. Grzesik, H. Qian, X.N. Xue, and J.W. Pollard. 2006. Macrophages regulate the angiogenic switch in a mouse model of breast cancer. *Cancer Res.* 66:11238–11246.
43. Paik, S., S. Shak, G. Tang, C. Kim, J. Baker, M. Cronin, F.L. Baehner, M.G. Walker, D. Watson, T. Park, et al. 2004. A multigene assay to predict recurrence of tamoxifen-treated, node-negative breast cancer. *N. Engl. J. Med.* 351:2817–2826.
44. Carmeliet, P. 2003. Angiogenesis in health and disease. *Nat. Med.* 9:653–660.
45. Fazzari, P., J. Penachioni, S. Gianola, F. Rossi, B.J. Eickholt, F. Maina, L. Alexopoulou, A. Sottile, P.M. Comoglio, R.A. Flavell, and L.

Tamagnone. 2007. Plexin-B1 plays a redundant role during mouse development and in tumour angiogenesis. *BMC Dev. Biol.* 7:55.
46. Knowles, H., R. Leek, and A.L. Harris. 2004. Macrophage infiltration and angiogenesis in human malignancy. *Novartis Found. Symp.* 256:189–200.
47. Talks, K.L., H. Turley, K.C. Gatter, P.H. Maxwell, C.W. Pugh, P.J. Ratcliffe, and A.L. Harris. 2000. The expression and distribution of the hypoxia-inducible factors HIF-1alpha and HIF-2alpha in normal human tissues, cancers, and tumor-associated macrophages. *Am. J. Pathol.* 157:411–421.
48. Cramer, T., Y. Yamanishi, B.E. Clausen, I. Forster, R. Pawlinski, N. Mackman, V.H. Haase, R. Jaenisch, M. Corr, V. Nizet, et al. 2003. HIF-1alpha is essential for myeloid cell-mediated inflammation. *Cell.* 112:645–657.
49. Pennacchietti, S., P. Michieli, M. Galluzzo, M. Mazzone, S. Giordano, and P.M. Comoglio. 2003. Hypoxia promotes invasive growth by transcriptional activation of the met protooncogene. *Cancer Cell.* 3:347–361.
50. Galimi, F., E. Cottone, E. Vigna, N. Arena, C. Boccaccio, S. Giordano, L. Naldini, and P.M. Comoglio. 2001. Hepatocyte growth factor is a regulator of monocyte-macrophage function. *J. Immunol.* 166:1241–1247.
51. Ray, B.K., A. Shakya, J.R. Turk, S.S. Apte, and A. Ray. 2004. Induction of the MMP-14 gene in macrophages of the atherosclerotic plaque: role of SAF-1 in the induction process. *Circ. Res.* 95:1082–1090.
52. Barberis, D., A. Casazza, R. Sordella, S. Corso, S. Artigiani, J. Settleman, P.M. Comoglio, and L. Tamagnone. 2005. p190 Rho-GTPase activating protein associates with plexins and it is required for semaphorin signalling. *J. Cell Sci.* 118:4689–4700.
53. Granziero, L., P. Circosta, C. Scielzo, E. Frisaldi, S. Stella, M. Geuna, S. Giordano, P. Ghia, and F. Caligaris-Cappio. 2003. CD100/Plexin-B1 interactions sustain proliferation and survival of normal and leukemic CD5+ B lymphocytes. *Blood.* 101:1962–1969.

nature immunology

REVIEW

Semaphorins and their receptors in immune cell interactions

Kazuhiro Suzuki[1,4], Atsushi Kumanogoh[2,3] & Hitoshi Kikutani[1,3]

Semaphorins are newcomers to the growing panoply of immunoregulatory proteins. Members of this family were originally identified as proteins that provide axonal guidance cues during neuronal development. However, accumulating evidence indicates that several semaphorins, called 'immune semaphorins', are crucial to various phases of the immune response, from initiation to terminal inflammatory processes. Extensive studies of immune semaphorins have shown not only differences but also parallels in semaphorin functions among physiologically distinct systems, providing unexpected but meaningful insights into the biological activities of this protein family. Here we review the present knowledge of the function of semaphorins and their receptors in the immune system, including the most recent advances in this field.

Since semaphorins were first described in the early 1990s, more than 20 types of these proteins have been identified as guidance factors that assist axon pathfinding during neuronal development[1,2]. Semaphorins have been also shown to have diverse and important functions in other physiological processes, including heart morphogenesis[3–7], vascular growth[4,5,8,9], tumor progression[10–13] and immune cell regulation[14]. In particular, understanding of the immunoregulatory functions of semaphorin family members has advanced considerably over the past several years.

Semaphorins are secreted and membrane-associated proteins characterized by a conserved amino-terminal 'Sema' domain. On the basis of structural elements and amino acid sequence similarity, this diverse group of proteins has been further divided into eight subclasses[15]. Invertebrate semaphorins are grouped into classes I and II, whereas classes III–VII are expressed in vertebrates[2]. In addition, some DNA viruses encode functional semaphorins that are assigned to class VIII (ref. 16). Semaphorins in classes I and IV–VII are membrane associated, whereas those in classes II and III and the viral semaphorins are secreted. Two groups of proteins, plexins and neuropilins, have been identified as the main receptors for semaphorins[17–21]. Most membrane-bound semaphorins directly bind plexins, whereas class III semaphorins require neuropilins as obligate coreceptors. However, it has been suggested that the receptor usage by semaphorins is more complex than previously thought. For example, Sema3E signals independently of neuropilin through plexin-D1 (ref. 8), and Sema7A uses integrin receptors to exert its function in both the nervous and immune systems[22,23]. In addition, two molecules unrelated to plexins and neuropilins, CD72 (ref. 24) and TIM-2 (T cell, immunoglobulin and mucin domain protein 2; ref. 25), functionally interact with class IV semaphorins in the immune system (**Fig. 1** and **Supplementary Table 1** online).

The immune response consists of a series of spatiotemporally well ordered cell-cell interactions, in which immune cells communicate bidirectionally and modulate the functions of interacting cells as well as themselves. So far, studies of the immune semaphorins have shown that several vertebrate and viral semaphorin family members are intimately involved in diverse immune cell interactions. Here we incorporate the present knowledge of immune semaphorins into the context of immune responses.

Sema4D and B cell function

The immune function of semaphorin molecules was first described in B cells through functional analysis of a class IV semaphorin, Sema4D. In the immune system, Sema4D is constitutively expressed on T cells[26,27]. Although B cells have low basal expression of Sema4D, it is upregulated considerably by various stimuli such as lipopolysaccharide and antibody to CD40 (ref. 24). The biological activity of Sema4D in B cells has been confirmed in both human and mouse systems. Transfectants that exogenously express human Sema4D promote the aggregation and survival of human B cells *in vitro*[28]. Recombinant mouse Sema4D and cells expressing Sema4D enhance the CD40- or lipopolysaccharide-induced proliferation and antibody production of mouse B cells[24]. The phenotypes of Sema4D-deficient mice, which have abnormal B cells and altered antibody responses[29], further support the idea that Sema4D is involved in B cell activation in the context of B cell–B cell and B cell–T cell interactions, as discussed below.

The receptor used by Sema4D differs in nonlymphoid versus lymphoid tissues. In the nervous system, Sema4D binds plexin-B1 and exerts chemorepulsive effects on various neurons[21,30,31]. In contrast, the C-type lectin CD72 serves as the functional Sema4D receptor in the

[1]Department of Molecular Immunology and Core Research for Evolutional Science and Technology program of the Japan Science and Technology Agency, [2]Department of Immunopathology, Research Institute for Microbial Diseases, and [3]World Premier International Immunology Frontier Research Center, Osaka University, Suita, Osaka 565-0871, Japan. [4]Present address: Howard Hughes Medical Institute and Department of Microbiology and Immunology, University of California, San Francisco, California 94143, USA. Correspondence should be addressed to H.K. (kikutani@ragtime.biken.osaka-u.ac.jp).

Published online 17 December 2007; doi:10.1038/ni1553

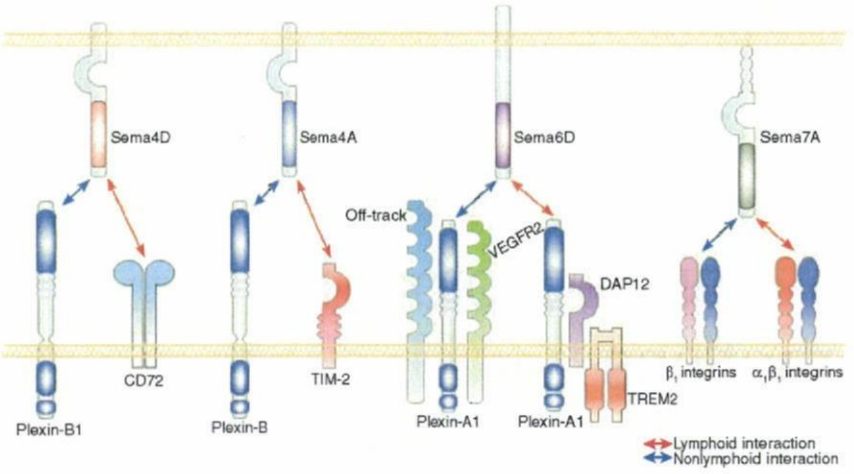

Figure 1 Immune semaphorins and their receptors in lymphoid and nonlymphoid cells. The class IV semaphorin Sema4D binds plexin-B1 and induces chemorepulsive signals in neuronal cells. In the immune system, however, Sema4D uses CD72 as a functional receptor and enhances the activation of B cells and DCs by diminishing inhibitory signals from CD72. Sema4A, another class IV semaphorin, binds TIM-2, and this interaction is critical for T cell activation and differentiation. Although Sema4A might interact with receptors belonging to plexin-B subfamily, the functional importance of these interactions remains unknown. Sema6D exerts different biological activities through plexin-A1, depending on its coreceptors. During chick embryogenesis, plexin-A1 differentially associates with off-track and VEGFR2, and these receptor complexes have distinct functions in heart development. In the immune system, plexin-A1 forms a receptor complex with TREM2 and DAP12 and, after Sema6D binds, this complex transduces signals that stimulate DCs and osteoclasts. The function of the glycosyl phosphatidylinositol-anchored semaphorin Sema7A is mediated through β_1 integrin receptors in both the nervous and immune systems. Sema7A expressed on activated T cells stimulates macrophages through $\alpha_1\beta_1$ integrin to promote inflammatory responses.

immune system[24]. CD72 contains two immunoreceptor tyrosine-based inhibitory motifs (ITIMs) in its cytoplasmic domain and functions as a negative regulator of B cells[32,33]. The regulatory function of CD72 is mediated by the tyrosine phosphatase SHP-1, which is recruited to the phosphorylated ITIMs of CD72. SHP-1 associates with the ITIM regions of several inhibitory receptors, such as CD22 and the KIRs (killer cell immunoglobulin-like receptors), induces dephosphorylation of their signaling proteins and inhibits immune cell activation[34–36]. Several lines of evidence indicate that Sema4D enhances B cell activation by turning off CD72 inhibitory signals. Indeed, both soluble Sema4D[24] and agonistic CD72-specific monoclonal antibodies[32,37] block tyrosine phosphorylation of CD72 and its association with SHP-1 in B cells stimulated with antibody to immunoglobin M. Furthermore, CD72 is constitutively phosphorylated and associated with SHP-1 in Sema4D-deficient B cells, which confers the hyporesponsiveness of these cells[29]. Moreover, Sema4D ligation inhibits the physical association of CD72 with the B cell receptor (BCR) complex[38]. This sequestration of CD72 away from the kinase-rich BCR signalosome might reduce CD72 phosphorylation. Therefore, Sema4D binding induces the dissociation of CD72 from the BCR complex, leading to dephosphorylation of the CD72 ITIM and dissociation of SHP-1 from CD72. This mechanism might be important for controlling the strength of BCR signals, but it remains unknown whether the same mechanism also accounts for the Sema4D-mediated regulation of CD40 or Toll-like receptor 4 signaling.

Several studies of mice with altered signaling molecules 'downstream' of the BCR have shown that changes in the BCR activation threshold affect B cell survival and turnover *in vivo*[39]. Indeed, Sema4D is involved in the homeostatic maintenance of B cell subsets. In young Sema4D-deficient mice, the $CD5^+$ B-1 cell population is smaller, although other B cell subsets seem normal[29]. However, as these mutant mice age, the proportion of $CD21^{hi}CD23^{lo}$ marginal zone B cells gradually increases[38]. Population expansion of marginal zone B cells is often found in mice with defective BCR signaling[39,40], whereas B-1 cell numbers are greater in mice lacking inhibitory receptors, including CD72 (refs. 41–43). This suggests that the requirements for BCR signaling vary among different B cell subsets. Therefore, the higher BCR signaling threshold in Sema4D-deficient mice may promote the development and survival of marginal zone B cells but may be detrimental for the development of B-1 cells. In homeostatic conditions, Sema4D is weakly expressed on resting B cells and might be involved in the maintenance of certain B cell subsets by 'fine tuning' BCR signals. In such circumstances, Sema4D signaling may occur through B cell–B cell interactions (**Fig. 2a**). Notably, the population expansion of marginal zone B cells in Sema4D-deficient mice is accompanied by the development of autoimmunity[38]. A variety of autoantibodies is detectable in the serum of these older mutant mice. Furthermore, leukocytes substantially infiltrate many tissues, including the salivary gland, liver and kidney. Notably, $CD21^{hi}CD23^{lo}$ marginal zone B cells comprise most of the infiltrating cells and are the main producers of autoantibodies.

In addition to a function in controlling B cell homeostasis, the profiles of Sema4D and CD72 expression in lymphocyte populations and the additional phenotypic characteristics of Sema4D-deficient mice suggest that the Sema4D-CD72 interaction is also involved in the development of B cell–mediated immunity. T cell–dependent antibody responses are initiated when B cells encounter helper T cells recognizing the same antigen at the boundary between B cell follicles and T cell zones in secondary lymphoid organs. Here, these cells engage in cognate interactions in which CD40-meditated signaling is indispensable for efficient B cell activation. Sema4D and CD72 are 'preferentially' expressed on T cells and B cells, respectively, and Sema4D enhances CD40-dependent B cell activation through CD72 (ref. 24). Moreover, T cell–dependent antibody responses are considerably impaired in Sema4D-deficient mice[29]. Given such observations, it is conceivable that Sema4D-CD72 interactions are involved in T cell–B cell interactions in the extrafollicular areas (**Fig. 2b**). Some activated B cells migrate into lymphoid follicles and form germinal centers where high-affinity B cells are selected with the provision of T cell–derived help. Sema4D expression in B cells is strongly induced by CD40 stimulation[24], and in fact Sema4D is reported to be expressed on germinal center B cells[28]. It is also noteworthy that Sema4D-deficient mice immunized with T cell–dependent antigens show defective antibody affinity maturation and poor generation of antigen-specific germinal center B cells[29]. Therefore, Sema4D-CD72 interactions might contribute to the population expansion of germinal center B cells through interactions between B cells (**Fig, 2a**) and support the selection of high-affinity B cells by enhancing survival signals from helper T cells (**Fig. 2b**).

Semaphorins and dendritic cell function

Extensive analyses of Sema4D-deficient mice have shown that Sema4D is also important in T cell–mediated immunity. After immunization with protein antigens, $CD4^+$ T cells from the draining lymph nodes of Sema4D-deficient mice show very impaired proliferative responses and cytokine production after antigen restimulation[29,44]. Moreover, Sema4D-deficient mice are resistant to experimental autoimmune encephalomyelitis (EAE) induced by myelin oligodendrocyte glycoprotein (MOG)–derived peptide, a phenotype ascribed to the defective generation of MOG-specific T cells[44]. Conversely, transgenic mice that overexpress soluble Sema4D have enhanced T cell responses[45]. These observations indicate that Sema4D is crucially involved in the initial activation and differentiation of T cells.

T cells are the main Sema4D-producing cells in the immune system. However, Sema4D-deficient T cells respond normally to CD3-specific monoclonal antibodies or mitogens such as concanavalin A[29], which suggests that Sema4D does not act in a T cell–autonomous way. Although it has been proposed that Sema4D functions as a receptor to assist the proliferative activity of human leukemic cells[46], Sema4D seems to act mainly as a ligand in the mouse immune system. Moreover, soluble recombinant Sema4D does not affect T cell activation[29], which suggests that Sema4D has no direct effect on T cells. In contrast, recombinant Sema4D enhances the surface expression of CD80, CD86 and major histocompatibility complex class II molecules on dendritic cells (DCs) and their immunogenicity that was induced by CD40 stimulation[44]. The function of Sema4D in T cell–DC interactions has been addressed with an *in vitro* experimental system[44]. Sema4D-sufficient T cell receptor (TCR)–transgenic $CD4^+$ T cells differentiate normally into cytokine-secreting effector cells even when cultured with antigen and Sema4D-deficient antigen-presenting cells. In contrast, Sema4D-deficient TCR-transgenic T cells fail to differentiate even in the presence of Sema4D-sufficient antigen-presenting cells. Therefore, Sema4D expressed on T cells acts on DCs to promote their activation and maturation, which in turn enhances T cell activation (**Fig. 3a**). Because most stimulatory effects of Sema4D on DCs are reproduced by agonistic CD72-specific monoclonal antibodies[44], DCs as well as B cells seem to use CD72 as their main Sema4D receptor.

Plexins have established functions as semaphorin receptors in the development of the nervous and cardiovascular systems[47]. However, their function in the immune system have not been addressed until recently. Plexin-A1 is one of the gene products induced by the CIITA transcription factor expressed in DCs and is involved in T cell–DC interactions[48]. 'Knockdown' of plexin-A1 by short hairpin RNA impairs the ability of a DC line to activate T cells *in vitro* and *in vivo*. The function of plexin-A1 in DC functions has been further substantiated through the generation and analysis of plexin-A1-deficient mice[49]. These mutant mice are resistant to MOG-induced EAE because of defective generation of MOG-specific T cells. This defect in T cell–mediated immunity is partially attributed to impaired DC function in these mice. Compared with wild-type DCs, plexin-A1-deficient DCs poorly stimulate allogeneic T cells or TCR-transgenic T cells in the presence of cognate antigens. These observations indicate that plexin-A1 expression in DCs is required for the efficient generation of antigen-specific T cells. In addition to its function in DC activation, plexin-A1 is also involved in osteoclast differentiation. Indeed, plexin-A1-deficient mice develop severe osteopetrosis due to decreased bone resorption that is attributed to defective osteoclastogenesis in these mice.

It is well established that plexin-A1 forms a receptor complex with neuropilin-1 to induce chemorepulsive signals of secreted class III semaphorins[2,20]. Additionally, plexin-A1 also serves as a receptor for Sema6D, a class VI transmembrane semaphorin, and contributes to cardiac morphogenesis[6,7]. Sema6D also functions as a ligand for plexin-A1 in the regulation of DC function[49]. Various lymphocyte populations, including T cells, B cells and natural killer cells, have relatively high expression of Sema6D mRNA. Recombinant Sema6D protein stimulates bone marrow–derived DCs to produce cytokines such as interleukin 12 (IL-12) and to increase expression of major histocompatibility complex class II molecules[49]. These activities and binding of Sema6D on DCs are profoundly attenuated in plexin-A1-deficient DCs[49]. Therefore, Sema6D expressed on T cells might stimulate DCs via plexin-A1 during T cell–DC interactions (**Fig. 3a**).

During chick cardiac morphogenesis, plexin-A1 differentially associates with two receptor-type tyrosine kinases, off-track and VEGFR2, and each receptor complex mediates distinct biological activities of Sema6D[6]. However, plexin-A1 on DCs associates with a complex of the receptor TREM2 and the adaptor DAP12 instead of off-track or VEGFR2 (ref. 49). DAP12 contains an immunoreceptor tyrosine-based activation motif in its cytoplasmic region, to which Src-like tyrosine kinases, including Zap70 and Syk, are recruited. In natural killer cells, DAP12 forms a complex with Ly49D, CD94-NKG2C and KIR2DS and acts as a signaling adaptor for these natural killer cell–activating receptors[50]. DAP12 also associates with TREM1 or TREM2, although the functions and ligands of these TREM proteins remain unknown[51]. In DCs, DAP12 associates with plexin-A1 indirectly through TREM2 (ref. 49). DCs treated with TREM2-specific small interfering RNA respond poorly to Sema6D stimulation, and

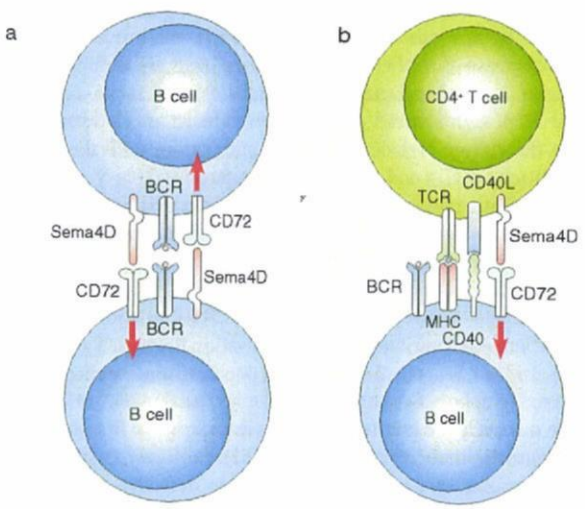

Figure 2 Sema4D in B cell–mediated immunity. (**a**) In homeostatic conditions, Sema4D is weakly expressed on B cells. In this setting, Sema4D-CD72 interactions between B cells might help maintain certain B cell subsets by 'fine tuning' BCR signals. Sema4D expression is strongly upregulated in germinal center B cells. This might enable high-avidity interactions of Sema4D with CD72, promoting the robust population expansion of germinal center B cells. (**b**) During T cell–dependent antibody responses, Sema4D abundantly expressed on $CD4^+$ T cells might be involved in the initial activation of follicular B cells in extrafollicular areas of secondary lymphoid organs by enhancing CD40-mediated signals. After germinal center formation, T cell–derived Sema4D might participate in the interaction between helper T cells and germinal center B cells, in which Sema4D signals might promote the survival of germinal center B cells and support efficient selection of high-affinity B cells. MHC, major histocompatibility complex.

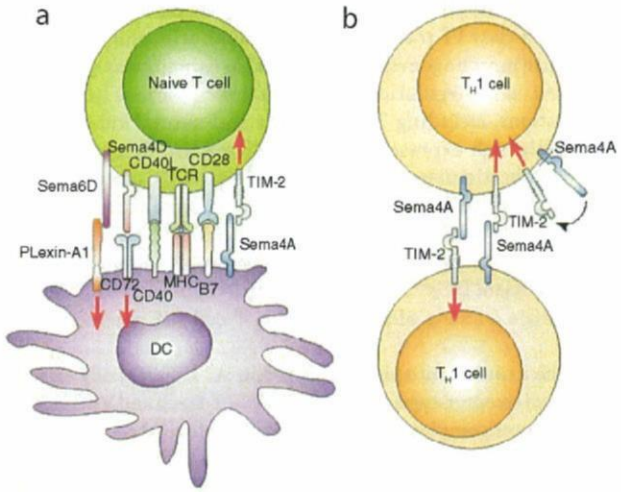

Figure 3 Involvement of semaphorins in T cell activation and differentiation. (**a**) In T cell–DC interactions, semaphorins mediate the reciprocal stimulation of T cells and DCs. The T cell–derived semaphorins Sema4D and Sema6D enhance DC activation and maturation through CD72 and a plexin-A1–TREM2–DAP12 complex, respectively. Conversely, Sema4A expressed on DCs directly stimulates T cells through TIM-2. These semaphorin signals might contribute to the optimal activation of antigen-specific T cells. (**b**) During the differentiation of $CD4^+$ T cells into cytokine-producing effector cells, Sema4A is selectively induced in T_H1 cells. The T_H1 cell–derived Sema4A further promotes T_H1 differentiation, which might be mediated by cognate cellular interactions between T_H1 cells and/or in an autocrine way.

DAP12-deficient DCs have a similar phenotype[49], which indicates that these adaptor molecules mediate Sema6D-induced plexin-A1 signaling.

Semaphorins and T cell activation, differentiation

Another member of the class IV semaphorin subfamily, Sema4A, also helps regulate T cell–mediated immune responses, but unlike Sema4D, Sema4A acts directly on T cells. The expression profile of Sema4A in immune cell populations is unique. Although there is constitutively high expression of Sema4A on the surfaces of all mouse DC subsets[25], its expression on T cells is tightly regulated[52]. After TCR stimulation, T cells transiently upregulate Sema4A within 24 hours, but its expression rapidly decreases thereafter. However, when T cells are stimulated in T helper type 1 (T_H1)–polarizing conditions containing IL-12 and antibody to IL-4, high Sema4A expression is induced and is sustained throughout the culture period. In contrast, stimulation with the T_H2-biasing conditions of IL-4 and antibody to interferon-γ (IFN-γ) induces only transient Sema4A expression. Notably, DC-derived Sema4A and T_H1 cell–derived Sema4A have distinct functions in the development of T cell–mediated immunity, as described below[52].

Recombinant Sema4A protein substantially enhances the proliferation and IL-2 production of naive T cells induced by TCR stimulation[25], which suggests that Sema4A contributes to T cell activation through T cell–DC interactions. Indeed, Sema4A-deficient DCs poorly stimulate allogeneic T cells in mixed lymphocyte culture, despite the fact that Sema4A-deficient DCs mature normally and produce cytokines in response to lipopolysaccharide or agonistic antibodies to CD40 (ref. 52). Consistent with those *in vitro* observations, Sema4A-deficient mice show defective generation of antigen-specific T cells after immunization with various antigens[52]. These observations indicate that Sema4A expressed on DCs is involved in the initial activation of T cells (**Fig. 3a**).

However, Sema4A expression in T cells is required for the differentiation of helper T cells. When cultured in T_H1-inducing conditions, Sema4A-deficient $CD4^+$ T cells fail to differentiate into IFN-γ–producing cells[52]. In contrast, Sema4A-deficient T cells differentiate normally into IL-4-producing cells in T_H2-inducing conditions. The selective defect in the T_H1 differentiation of Sema4A-deficient T cells is associated with lower expression of the IL-12 receptor β2 chain and T-bet, a transcription factor essential for T_H1 development[53]. Notably, the impaired T_H1 differentiation of Sema4A-deficient T cells is fully restored with recombinant Sema4A protein or wild-type T cells[52]. Therefore, Sema4A expressed on T cells might promote T_H1 differentiation through cognate interactions between T cells and/or an autocrine pathway (**Fig. 3b**). Furthermore, the involvement of Sema4A in the regulation of helper T cell differentiation has been confirmed *in vivo*. The generation of IFN-γ-producing antigen-specific T cells is impaired in Sema4A-deficient mice immunized with T_H1-inducing agents such as heat-killed *Propionibacterium acnes*[52]. Conversely, when infected with *Nippostrongylus brasiliensis*, a T_H2-inducing intestinal nematode, Sema4A-deficient mice mount enhanced T_H2 responses relative to those of wild-type mice[52]. Moreover, Sema4A-deficient mice of a T_H2-prone BALB/c strain spontaneously develop atopic dermatitis (unpublished data).

The functions of DC-derived and T cell–derived Sema4A have been delineated in transfer experiments with antigen-pulsed DCs[52]. When Sema4A-deficient DCs are transferred into Sema4A-sufficient mice, antigen-specific T cells show impaired proliferation and IL-2 secretion, but substantial numbers of IFN-γ-producing T cells are generated. In contrast, there is a selective defect in IFN-γ production but not in the proliferation and IL-2 production of antigen-specific T cells in Sema4A-deficient mice receiving Sema4A-sufficient DCs. These *in vivo* observations define distinct functions for Sema4A expressed by two different immune cell subsets: DC-derived Sema4A is essential for T cell priming, and T cell–derived Sema4A is required for T_H1 differentiation.

TIM-2, which belongs to the TIM family[54], was identified as a Sema4A receptor by expression cloning with a mouse T cell cDNA library[25]. Because Sema4A binding induces tyrosine phosphorylation of the cytoplasmic tail of TIM-2, TIM-2 seems to transduce Sema4A signals[25]. Studies have suggested involvement of TIM-2 in the regulation of helper T cell activities. Administration of recombinant TIM-2 protein suppresses the development of EAE in SJL mice immunized with proteolipid protein–derived peptide by inhibiting the generation of T_H1 cells[55]. In a model of airway atopy, TIM-2-deficient mice show exacerbated lung inflammation accompanied by dysregulated T_H2 responses[56]. These findings support the idea that TIM-2 serves as a functional receptor for Sema4A. However, although the main phenotypes of TIM-2- and Sema4A-deficient mice are similar, there are some inconsistencies. For example, T cells from TIM-2-deficient mice but not those from Sema4A-deficient mice show enhanced basal proliferation. Thus, it is likely that Sema4A or TIM-2 has another binding partner in the immune system. Like other class IV semaphorins, Sema4A has the ability to bind several plexin molecules, including the members of the plexin-B subfamily and plexin-D1 (ref. 57), some of which are expressed by T cells (unpublished data). Thus, it is conceivable that Sema4A acts on T cells through these plexin molecules.

In addition to Sema4A, several lines of evidence suggest that a secreted class III semaphorin, Sema3A, also regulates T cell functions. Sema3A is produced by DCs[58] and various types of tumor cells[59]. Treating T cells with recombinant or tumor-derived Sema3A inhibits TCR-mediated proliferation and cytokine production by downregulating mitogen-activated protein kinase signaling cascades, although the receptor system for Sema3A in T cells remains unidentified[58,59]. These observations suggest that Sema3A serves as a negative regulator for T cells in physiological and pathological immune responses. Although there is a report that a class

VII semaphorin, Sema7A, suppresses T cell activation in a cell-autonomous way[60], the observations in that report remain controversial. Instead, Sema7A expressed on T cells has been shown to have a positive regulatory function in the immune system, as described below[23].

Semaphorins and inflammatory responses

In the later phase of T cell–mediated immunity, antigen-specific effector T cells trigger inflammatory responses by activating macrophages in peripheral tissues. This activation of macrophages is promoted by both secreted and cell-associated factors from effector T cells, including IFN-γ and CD40 ligand (CD40L), which leads to pathogen elimination at the site of infection but can also lead to tissue destruction in autoimmune or allergic diseases[61]. A study has shown that Sema7A, a membrane-associated glycosylphosphatidylinositol-linked semaphorin, is important in this process[23].

Sema7A transcripts are detectable in the embryonic nervous system and in adult tissues, including the brain, spinal cord, lung and secondary lymphoid organs[62–64]. Among lymphocyte populations, Sema7A is expressed mainly in activated T cells[23]. Notably, the Sema domain of Sema7A contains an arginine-glycine-aspartate sequence that is a well conserved integrin-binding motif[65]. In accordance with that finding, a neurological study has shown that Sema7A promotes axon outgrowth through β_1 integrin receptors by activating the 'downstream' mitogen-activated protein kinase pathway and contributes to the formation of lateral olfactory tracts[22].

In the immune system, Sema7A expressed on activated T cells stimulates macrophages to produce proinflammatory cytokines through the $\alpha_1\beta_1$ integrin[23]. Thus, integrin-mediated signaling is a common mechanism by which Sema7A functions in both the nervous and immune systems. As a glycosylphosphatidylinositol-anchored protein, Sema7A is recruited to lipid rafts that accumulate at the immunological synapse between T cells and macrophages, where it interacts with $\alpha_1\beta_1$ integrin[23]. So far, $\alpha_1\beta_1$ integrin has been identified as a collagen receptor and as an 'anchor' that interacts with the extracellular matrix to retain effector cells at sites of inflammation[66–69]. Thus, Sema7A interacts with $\alpha_1\beta_1$ integrin in a totally different way than collagens do and might deliver stimulatory signals to macrophages more efficiently through the specialized signaling module.

Sema7A-deficient mice are defective in T cell–mediated immune responses such as contact hypersensitivity and EAE[23]. Detailed *in vivo* analyses have indicated that Sema7A deficiency does not affect the generation of antigen-specific effector T cells and their migration into inflammatory sites. However, Sema7A-deficient T cells fail to induce contact hypersensitivity responses when directly introduced into the antigen-challenged site. Therefore, the interaction of Sema7A with $\alpha_1\beta_1$ integrin is crucial for T cell–mediated macrophage activation at sites of inflammation. It has been reported that Sema7A is involved in the pathogenesis of lung fibrosis induced by transforming growth factor-β1 (ref. 70). In this disease development, transforming growth factor-β1 activates phosphatidylinositol 3-OH kinase and its downstream component protein kinase B (Akt) in a Sema7A-dependent way. Given the importance of the phosphatidylinositol 3-OH kinase–protein kinase B (Akt) pathway in integrin-mediated signaling[65], it is possible that Sema7A is involved in this disease model by means of integrin receptors.

This newly identified immune function of Sema7A provides insight into the mechanism by which effector T cells induce inflammation through macrophage activation. In the conventional model of T cell–mediated inflammation, IFN-γ and CD40L are the most potent effector molecules that promote inflammatory programs in macrophages[61]. However, these factors are synthesized anew in T cells only after antigen recognition on macrophages, a process that requires several hours[61]. Moreover, the induction of CD40 on macrophages requires IFN-γ produced by activated T cells[71]. In contrast, high expression of Sema7A is maintained on effector T cells after they differentiate from naive T cells[23]. Thus, it is conceivable that Sema7A helps initiate inflammatory cascades by stimulating cytokine production by macrophages, and its adhesive interactions with $\alpha_1\beta_1$ integrin support firm contacts between effector T cells and macrophages, ensuring efficient induction and action of IFN-γ and CD40L (**Fig. 4**). In addition to the direct activation of macrophages, effector T cells are also involved in the recruitment of macrophages into inflammatory sites by producing chemokines such as CCL2 (ref. 61). An *in vitro* study has shown that recombinant soluble Sema7A acts as chemoattractant for monocytes with much more potency than canonical chemokines[72], which suggests that Sema7A derived from effector T cells promotes macrophage recruitment to sites of inflammation.

Other semaphorins are also thought to participate in inflammatory immune responses. Indeed, recombinant human class IV semaphorins induce cytokine production from monocytes, although their precise functions in inflammation remain elusive[73]. Furthermore, a vaccinia virus semaphorin, A39R, binds plexin-C1 and induces robust responses in human monocytes, including aggregation and cytokine production[17]. It is possible that infected cells express and secrete this virus semaphorin to enhance inflammatory responses and exacerbate disease by activating the host immune system.

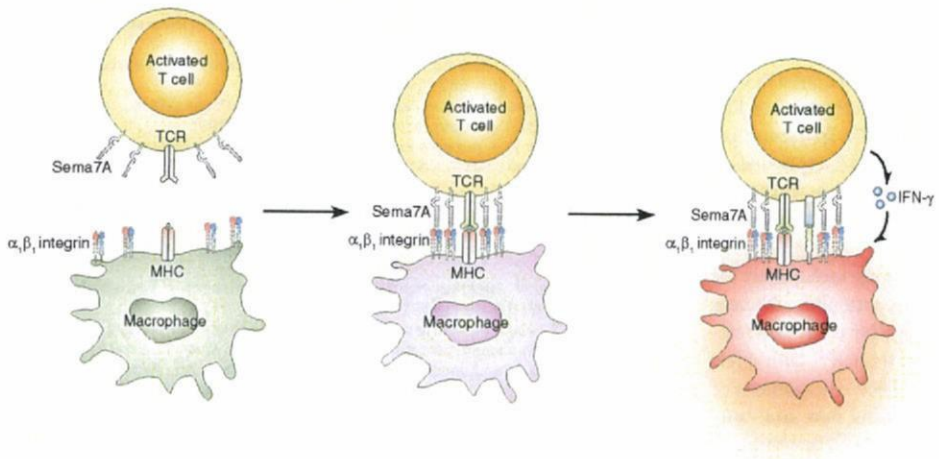

Figure 4 A model for Sema7A function in T cell–mediated inflammation. Sema7A is a glycosylphosphatidylinositol-anchored protein whose expression on T cells is sustained in large amounts once the cells are activated. When tissue-infiltrating effector T cells encounter macrophages, Sema7A on T cells is rapidly redistributed to the immunological synapse along with lipid rafts and induces clustering of $\alpha_1\beta_1$ integrin on macrophages. The Sema7A signals mediated by $\alpha_1\beta_1$ integrin stimulate macrophages to produce proinflammatory cytokines and trigger inflammatory processes at peripheral tissues. The interaction of Sema7A with $\alpha_1\beta_1$ integrin might also promote firm adhesion between T cells and macrophages. Macrophage activation by Sema7A is followed by the action of CD40L and IFN-γ, both of which are induced in effector T cells only after antigen recognition on macrophages and further promote inflammation.

Concluding remarks and future directions

As described above, accumulating evidence has identified the semaphorin family as a new class of immunoregulatory molecules. Although detailed analyses have been made of only a limited number of family members, they actively participate in various aspects of the immune response by several distinct mechanisms. Beyond the basic implications, studies of immune semaphorins have provided valuable insights into therapeutic strategies for autoimmune and allergic diseases, as involvement of semaphorins in the pathogenesis of these immune disorders has been demonstrated in several animal models[23,25,44,49].

However, resolution of an important issue remains elusive. So far, most of the immunological studies of semaphorins have focused on their costimulatory effects on immune cells. In the nervous and cardiovascular systems; however, semaphorins have established functions in regulating cell motility and morphology through receptors belonging to the plexin family[47]. In addition, emerging evidence suggests that there are two convergent mechanisms by which semaphorin-plexin signaling affects these aspects of cellular functions[47]. One is the regulation of actin cytoskeleton through GTPases of the Rho family, such as Rho and Rac, and the other is the modulation of integrin-mediated cell adhesion that involves a Ras-family GTPase, R-Ras. However, the function of semaphorins in regulating the migration and adhesive interaction of immune cells has been poorly elucidated.

Several aspects of immune responses, including the transmigration of leukocytes through vascular endothelium and the formation of immunological synapses, are heavily dependent on cytoskeletal dynamics and integrin activity[74–76]. Thus, it is reasonable that semaphorins might use plexin receptors to regulate the migration and adhesion of immune cells and therefore are involved in these key steps of immune responses. Indeed, there are data supporting that hypothesis. It has been reported that recombinant soluble Sema4D inhibits the migration of B cells, monocytes and immature DCs[77,78]. In DCs, this effect seems to be mediated by plexin-B1, a canonical Sema4D receptor in the nervous system[77]. In addition, the virus-encoded semaphorin A39R suppresses the integrin-mediated adhesion and migration of DCs by means of plexin-C1 (ref. 79). Moreover, Sema6D induces activation of Rac GTPase in DCs[49], which suggests that the Sema6D–plexin-A1 interaction regulates cytoskeletal events in DCs. Because activation of Rac GTPases in DCs is essential for dendrite extensions and contacts with naive T cells[80], it is possible that Sema6D-induced activation of Rac GTPases facilitates the initial scanning of T cells by DCs. In the context of T cell–DC interactions, it is also possible that Sema4A expressed on DCs affects actin-mediated receptor redistribution and integrin activities on the T cell side of the immunological synapse, ensuring optimal T cell activation.

At present there is a surge of innovation in imaging technology for the *in situ* visualization of the immune system. In particular, advances in multiphoton-excited laser-scanning microscopy have allowed real-time imaging of immune cells in living lymphoid tissues[81]. Only a few years after the introduction of this technology, various components of the immune response have been visualized, providing new and valuable insights into fundamental ideas in immunology[82,83]. In combination with conventional experimental methods, this powerful imaging technique could be instrumental in addressing the precise function of semaphorins in regulating immune cell dynamics in a complex physiological milieu. Although studies of immune semaphorins so far have described differences rather than similarities in semaphorin functions among physiologically distinct systems, identifying the unifying principle of semaphorin signaling that operates throughout the body will lead to comprehensive understanding of this interesting family of proteins.

Note: Supplementary information is available on the Nature Immunology website.

ACKNOWLEDGMENTS

We thank K. Kubota for secretarial assistance and N. Takegahara for artwork. Supported by the Ministry of Education, Culture, Sports, Science and Technology of Japan and the Core Research for Evolutional Science and Technology program of the Japanese Science and Technology Agency (H.K.); the Program for Promotion of Fundamental Studies in Health Science of the National Institute of Biomedical Innovation and the Target Protein Research Program of the Japan Science and Technology Agency (A.K.); and Research Fellowships of the Japan Society for the Promotion of Science for Young Scientists (K.S.).

Published online at http://www.nature.com/natureimmunology
Reprints and permissions information is available online at http://npg.nature.com/reprintsandpermissions

1. Kolodkin, A.L., Matthes, D.J. & Goodman, C.S. The semaphorin genes encode a family of transmembrane and secreted growth cone guidance molecules. *Cell* **75**, 1389–1399 (1993).
2. Pasterkamp, R.J. & Kolodkin, A.L. Semaphorin junction: making tracks toward neural connectivity. *Curr. Opin. Neurobiol.* **13**, 79–89 (2003).
3. Behar, O., Golden, J.A., Mashimo, H., Schoen, F.J. & Fishman, M.C. Semaphorin III is needed for normal patterning and growth of nerves, bones and heart. *Nature* **383**, 525–528 (1996).
4. Gitler, A.D., Lu, M.M. & Epstein, J.A. PlexinD1 and semaphorin signaling are required in endothelial cells for cardiovascular development. *Dev. Cell* **7**, 107–116 (2004).
5. Gu, C. *et al.* Neuropilin-1 conveys semaphorin and VEGF signaling during neural and cardiovascular development. *Dev. Cell* **5**, 45–57 (2003).
6. Toyofuku, T. *et al.* Dual roles of Sema6D in cardiac morphogenesis through region-specific association of its receptor, Plexin-A1, with off-track and vascular endothelial growth factor receptor type 2. *Genes Dev.* **18**, 435–447 (2004).
7. Toyofuku, T. *et al.* Guidance of myocardial patterning in cardiac development by Sema6D reverse signalling. *Nat. Cell Biol.* **6**, 1204–1211 (2004).
8. Gu, C. *et al.* Semaphorin 3E and plexin-D1 control vascular pattern independently of neuropilins. *Science* **307**, 265–268 (2005).
9. Serini, G. *et al.* Class 3 semaphorins control vascular morphogenesis by inhibiting integrin function. *Nature* **424**, 391–397 (2003).
10. Sekido, Y. *et al.* Human semaphorins A(V) and IV reside in the 3p21.3 small cell lung cancer deletion region and demonstrate distinct expression patterns. *Proc. Natl. Acad. Sci. USA* **93**, 4120–4125 (1996).
11. Tomizawa, Y. *et al.* Inhibition of lung cancer cell growth and induction of apoptosis after reexpression of 3p21.3 candidate tumor suppressor gene SEMA3B. *Proc. Natl. Acad. Sci. USA* **98**, 13954–13959 (2001).
12. Tse, C., Xiang, R.H., Bracht, T. & Naylor, S.L. Human Semaphorin 3B (SEMA3B) located at chromosome 3p21.3 suppresses tumor formation in an adenocarcinoma cell line. *Cancer Res.* **62**, 542–546 (2002).
13. Xiang, R. *et al.* Semaphorin 3F gene from human 3p21.3 suppresses tumor formation in nude mice. *Cancer Res.* **62**, 2637–2643 (2002).
14. Kikutani, H., Suzuki, K. & Kumanogoh, A. Immune semaphorins: increasing members and their diverse roles. *Adv. Immunol.* **93**, 121–143 (2007).
15. Semaphorin Nomenclature Committee. Unified nomenclature for the semaphorins/collapsins. *Cell* **97**, 551–552 (1999).
16. Spriggs, M.K. Shared resources between the neural and immune systems: semaphorins join the ranks. *Curr. Opin. Immunol.* **11**, 387–391 (1999).
17. Comeau, M.R. *et al.* A poxvirus-encoded semaphorin induces cytokine production from monocytes and binds to a novel cellular semaphorin receptor, VESPR. *Immunity* **8**, 473–482 (1998).
18. He, Z. & Tessier-Lavigne, M. Neuropilin is a receptor for the axonal chemorepellent Semaphorin III. *Cell* **90**, 739–751 (1997).
19. Kolodkin, A.L. *et al.* Neuropilin is a semaphorin III receptor. *Cell* **90**, 753–762 (1997).
20. Takahashi, T. *et al.* Plexin-neuropilin-1 complexes form functional semaphorin-3A receptors. *Cell* **99**, 59–69 (1999).
21. Tamagnone, L. *et al.* Plexins are a large family of receptors for transmembrane, secreted, and GPI-anchored semaphorins in vertebrates. *Cell* **99**, 71–80 (1999).
22. Pasterkamp, R.J., Peschon, J.J., Spriggs, M.K. & Kolodkin, A.L. Semaphorin 7A promotes axon outgrowth through integrins and MAPKs. *Nature* **424**, 398–405 (2003).
23. Suzuki, K. *et al.* Semaphorin 7A initiates T-cell-mediated inflammatory responses through alpha1beta1 integrin. *Nature* **446**, 680–684 (2007).
24. Kumanogoh, A. *et al.* Identification of CD72 as a lymphocyte receptor for the class IV semaphorin CD100: a novel mechanism for regulating B cell signaling. *Immunity* **13**, 621–631 (2000).
25. Kumanogoh, A. *et al.* Class IV semaphorin Sema4A enhances T-cell activation and interacts with Tim-2. *Nature* **419**, 629–633 (2002).
26. Bougeret, C. *et al.* Increased surface expression of a newly identified 150-kDa dimer early after human T lymphocyte activation. *J. Immunol.* **148**, 318–323 (1992).
27. Delaire, S., Elhabazi, A., Bensussan, A. & Boumsell, L. CD100 is a leukocyte semaphorin. *Cell. Mol. Life Sci.* **54**, 1265–1276 (1998).
28. Hall, K.T. *et al.* Human CD100, a novel leukocyte semaphorin that promotes B-cell aggregation and differentiation. *Proc. Natl. Acad. Sci. USA* **93**, 11780–11785 (1996).

29. Shi, W. *et al.* The class IV semaphorin CD100 plays nonredundant roles in the immune system: defective B and T cell activation in CD100-deficient mice. *Immunity* **13**, 633–642 (2000).
30. Oinuma, I., Ishikawa, Y., Katoh, H. & Negishi, M. The Semaphorin 4D receptor Plexin-B1 is a GTPase activating protein for R-Ras. *Science* **305**, 862–865 (2004).
31. Swiercz, J.M., Kuner, R., Behrens, J. & Offermanns, S. Plexin-B1 directly interacts with PDZ-RhoGEF/LARG to regulate RhoA and growth cone morphology. *Neuron* **35**, 51–63 (2002).
32. Adachi, T., Flaswinkel, H., Yakura, H., Reth, M. & Tsubata, T. The B cell surface protein CD72 recruits the tyrosine phosphatase SHP-1 upon tyrosine phosphorylation. *J. Immunol.* **160**, 4662–4665 (1998).
33. Adachi, T. *et al.* SHP-1 requires inhibitory co-receptors to down-modulate B cell antigen receptor-mediated phosphorylation of cellular substrates. *J. Biol. Chem.* **276**, 26648–26655 (2001).
34. Doody, G.M. *et al.* A role in B cell activation for CD22 and the protein tyrosine phosphatase SHP. *Science* **269**, 242–244 (1995).
35. Somani, A.K. *et al.* The SH2 domain containing tyrosine phosphatase-1 down-regulates activation of Lyn and Lyn-induced tyrosine phosphorylation of the CD19 receptor in B cells. *J. Biol. Chem.* **276**, 1938–1944 (2001).
36. Tonks, N.K. & Neel, B.G. From form to function: signaling by protein tyrosine phosphatase. *Cell* **87**, 365–368 (1996).
37. Wu, Y. *et al.* The B-cell transmembrane protein CD72 binds to and is an in vivo substrate of the protein tyrosine phosphatase SHP-1. *Curr. Biol.* **8**, 1009–1017 (1998).
38. Kumanogoh, A. *et al.* Requirement for CD100–CD72 interactions in fine-tuning of B-cell antigen receptor signaling and homeostatic maintenance of the B-cell compartment. *Int. Immunol.* **17**, 1277–1282 (2005).
39. Niiro, H. & Clark, E.A. Regulation of B-cell fate by antigen-receptor signals. *Nat. Rev. Immunol.* **2**, 945–956 (2002).
40. Kurosaki, T. Regulation of B cell fates by BCR signaling components. *Curr. Opin. Immunol.* **14**, 341–347 (2002).
41. O'Keefe, T.L., Williams, G.T., Davies, S.L. & Neuberger, M.S. Hyperresponsive B cells in CD22-deficient mice. *Science* **274**, 798–801 (1996).
42. Pan, C., Baumgarth, N. & Parnes, J.R. CD72-deficient mice reveal nonredundant roles of CD72 in B cell development and activation. *Immunity* **11**, 495–506 (1999).
43. Sato, S. *et al.* CD22 is both a positive and negative regulator of B lymphocyte antigen receptor signal transduction: altered signaling in CD22-deficient mice. *Immunity* **5**, 551–562 (1996).
44. Kumanogoh, A. *et al.* Requirement for the lymphocyte semaphorin, CD100, in the induction of antigen-specific T cells and the maturation of dendritic cells. *J. Immunol.* **169**, 1175–1181 (2002).
45. Watanabe, C. *et al.* Enhanced immune responses in transgenic mice expressing a truncated form of the lymphocyte semaphorin cd100. *J. Immunol.* **167**, 4321–4328 (2001).
46. Granziero, L. *et al.* CD100/Plexin-B1 interactions sustain proliferation and survival of normal and leukemic CD5$^+$ B lymphocytes. *Blood* **101**, 1962–1969 (2003).
47. Kruger, R.P., Aurandt, J. & Guan, K.L. Semaphorins command cells to move. *Nat. Rev. Mol. Cell Biol.* **6**, 789–800 (2005).
48. Wong, A.W. *et al.* CIITA-regulated plexin-A1 affects T-cell-dendritic cell interactions. *Nat. Immunol.* **4**, 891–898 (2003).
49. Takegahara, N. *et al.* Plexin-A1 and its interaction with DAP12 in immune responses and bone homeostasis. *Nat. Cell Biol.* **8**, 615–622 (2006).
50. Lanier, L.L. & Bakker, A.B. The ITAM-bearing transmembrane adaptor DAP12 in lymphoid and myeloid cell function. *Immunol. Today* **21**, 611–614 (2000).
51. Colonna, M. TREMs in the immune system and beyond. *Nat. Rev. Immunol.* **3**, 445–453 (2003).
52. Kumanogoh, A. *et al.* Nonredundant roles of Sema4A in the immune system: defective T cell priming and Th1/Th2 regulation in Sema4A-deficient mice. *Immunity* **22**, 305–316 (2005).
53. Szabo, S.J. *et al.* A novel transcription factor, T-bet, directs Th1 lineage commitment. *Cell* **100**, 655–669 (2000).
54. Kuchroo, V.K., Meyers, J.H., Umetsu, D.T. & DeKruyff, R.H. TIM family of genes in immunity and tolerance. *Adv. Immunol.* **91**, 227–249 (2006).
55. Chakravarti, S. *et al.* Tim-2 regulates T helper type 2 responses and autoimmunity. *J. Exp. Med.* **202**, 437–444 (2005).
56. Rennert, P.D. *et al.* T cell, Ig domain, mucin domain-2 gene-deficient mice reveal a novel mechanism for the regulation of Th2 immune responses and airway inflammation. *J. Immunol.* **177**, 4311–4321 (2006).
57. Toyofuku, T. *et al.* Semaphorin-4A, an activator for T-cell-mediated immunity, suppresses angiogenesis via plexin-D1. *EMBO J.* **26**, 1373–1384 (2007).
58. Lepelletier, Y. *et al.* Immunosuppressive role of semaphorin-3A on T cell proliferation is mediated by inhibition of actin cytoskeleton reorganization. *Eur. J. Immunol.* **36**, 1782–1793 (2006).
59. Catalano, A. *et al.* Semaphorin-3A is expressed by tumor cells and alters T-cell signal transduction and function. *Blood* **107**, 3321–3329 (2006).
60. Czopik, A.K., Bynoe, M.S., Palm, N., Raine, C.S. & Medzhitov, R. Semaphorin 7A is a negative regulator of T cell responses. *Immunity* **24**, 591–600 (2006).
61. Janeway, C.A. Jr, Travers, P., Walport, M. & Schlomchik, M.J. in *Immunobiology: the Immune System in Health and Disease* 6th edn. (ed. Janeway, C.A., Jr.) 357–361 (Garland Science Publishing, New York, 2005).
62. Mine, T. *et al.* CDw108 expression during T-cell development. *Tissue Antigens* **55**, 429–436 (2000).
63. Xu, X. *et al.* Human semaphorin K1 is glycosylphosphatidylinositol-linked and defines a new subfamily of viral-related semaphorins. *J. Biol. Chem.* **273**, 22428–22434 (1998).
64. Yamada, A. *et al.* Molecular cloning of a glycosylphosphatidylinositol-anchored molecule CDw108. *J. Immunol.* **162**, 4094–4100 (1999).
65. Hynes, R.O. Integrins: bidirectional, allosteric signaling machines. *Cell* **110**, 673–687 (2002).
66. Andreasen, S.O. *et al.* Expression and functional importance of collagen-binding integrins, $\alpha_1\beta_1$ and $\alpha_2\beta_1$, on virus-activated T cells. *J. Immunol.* **171**, 2804–2811 (2003).
67. Ben-Horin, S. & Bank, I. The role of very late antigen-1 in immune-mediated inflammation. *Clin. Immunol.* **113**, 119–129 (2004).
68. Hemler, M.E. VLA proteins in the integrin family: structures, functions, and their role on leukocytes. *Annu. Rev. Immunol.* **8**, 365–400 (1990).
69. Ray, S.J. *et al.* The collagen binding $\alpha_1\beta_1$ integrin VLA-1 regulates CD8 T cell-mediated immune protection against heterologous influenza infection. *Immunity* **20**, 167–179 (2004).
70. Kang, H.R., Lee, C.G., Homer, R.J. & Elias, J.A. Semaphorin 7A plays a critical role in TGF-β1-induced pulmonary fibrosis. *J. Exp. Med.* **204**, 1083–1093 (2007).
71. Alderson, M.R. *et al.* CD40 expression by human monocytes: regulation by cytokines and activation of monocytes by the ligand for CD40. *J. Exp. Med.* **178**, 669–674 (1993).
72. Holmes, S. *et al.* Sema7A is a potent monocyte stimulator. *Scand. J. Immunol.* **56**, 270–275 (2002).
73. Ishida, I. *et al.* Involvement of CD100, a lymphocyte semaphorin, in the activation of the human immune system via CD72: implications for the regulation of immune and inflammatory responses. *Int. Immunol.* **15**, 1027–1034 (2003).
74. Billadeau, D.D., Nolz, J.C. & Gomez, T.S. Regulation of T-cell activation by the cytoskeleton. *Nat. Rev. Immunol.* **7**, 131–143 (2007).
75. Ley, K., Laudanna, C., Cybulsky, M.I. & Nourshargh, S. Getting to the site of inflammation: the leukocyte adhesion cascade updated. *Nat. Rev. Immunol.* **7**, 678–689 (2007).
76. Vicente-Manzanares, M. & Sanchez-Madrid, F. Role of the cytoskeleton during leukocyte responses. *Nat. Rev. Immunol.* **4**, 110–122 (2004).
77. Chabbert-de Ponnat, I. *et al.* Soluble CD100 functions on human monocytes and immature dendritic cells require plexin C1 and plexin B1, respectively. *Int. Immunol.* **17**, 439–447 (2005).
78. Delaire, S. *et al.* Biological activity of soluble CD100. II. Soluble CD100, similarly to H-SemaIII, inhibits immune cell migration. *J. Immunol.* **166**, 4348–4354 (2001).
79. Walzer, T., Galibert, L., Comeau, M.R. & De Smedt, T. Plexin C1 engagement on mouse dendritic cells by viral semaphorin A39R induces actin cytoskeleton rearrangement and inhibits integrin-mediated adhesion and chemokine-induced migration. *J. Immunol.* **174**, 51–59 (2005).
80. Benvenuti, F. *et al.* Requirement of Rac1 and Rac2 expression by mature dendritic cells for T cell priming. *Science* **305**, 1150–1153 (2004).
81. Germain, R.N., Miller, M.J., Dustin, M.L. & Nussenzweig, M.C. Dynamic imaging of the immune system: progress, pitfalls and promise. *Nat. Rev. Immunol.* **6**, 497–507 (2006).
82. Allen, C.D., Okada, T. & Cyster, J.G. Germinal-center organization and cellular dynamics. *Immunity* **27**, 190–202 (2007).
83. Mempel, T.R., Scimone, M.L., Mora, J.R. & von Andrian, U.H. In vivo imaging of leukocyte trafficking in blood vessels and tissues. *Curr. Opin. Immunol.* **16**, 406–417 (2004).

Neuroscience Research 64 (2009) 152–161

Contents lists available at ScienceDirect

Neuroscience Research

journal homepage: www.elsevier.com/locate/neures

Membrane potential response profiles of CA1 pyramidal cells probed with voltage-sensitive dye optical imaging in rat hippocampal slices reveal the impact of $GABA_A$-mediated feed-forward inhibition in signal propagation

Yoko Tominaga [a,c], Michinori Ichikawa [c,1], Takashi Tominaga [a,b,c,*]

[a] Department of Neurophysiology, Kagawa School of Pharmaceutical Sciences, Tokushima Bunri University, 1314-1 Shido, Sanuki, Kagawa 769-2193, Japan
[b] Laboratory for Dynamics of Emergent Intelligence, RIKEN Brain Science Institute (BSI), 2-1 Hirosawa, Wako, Saitama 351-0198, Japan
[c] Laboratory for Brain-Operative Devices, RIKEN Brain Science Institute (BSI), 2-1 Hirosawa, Wako, Saitama 351-0198, Japan

ARTICLE INFO

Article history:
Received 30 April 2008
Received in revised form 17 February 2009
Accepted 19 February 2009
Available online 5 March 2009

Keywords:
Dendrite
Integration
Action potential firing
Computer simulation

ABSTRACT

The spatial and temporal distribution of excitatory and inhibitory membrane potential responses on a cell plays an important role in neuronal calculations in local neuronal circuits in the brain. The electrical dynamics of excitatory and inhibitory inputs along the somatodendritic extent of CA1 pyramidal cells during circuit activation were examined by stimulating strata radiatum (SR), oriens (SO), and lacunosum-moleculare (SLM) and measuring laminar responses with voltage-sensitive dye (VSD) optical recording methods. We first confirmed the linearity of the optical signal by comparing fluorescence changes in CA1 to global membrane potential changes when slices were bathed in high-potassium ($[K^+]_O$ = 25 mM) solution. Except for a TTX-sensitive component in stratum pyramidale, fluorescence changes were equal in all strata, indicating that VSD sensitivity had reasonable linearity across layers. We then compared membrane potential profiles in slices exposed to picrotoxin, a $GABA_A$ receptor antagonist. We attributed the picrotoxin-induced changes in the first peak of the excitatory membrane potential to feed-forward inhibition and the later response (appearing 30 ms after stimulation) to feedback inhibition. A difference in feed-forward components was observed in perisomatic and distal apical dendritic regions after SR stimulation. SLM stimulation produced large differences in perisomatic and apical dendritic regions. SO stimulation, however, produced no feed-forward inhibition at the perisomatic region, but produces feed-forward inhibition in distal dendritic regions. These results suggest that actual inhibition of membrane potential response by feed-forward inhibition is greater at perisomatic regions after SR or SLM stimulation but is smaller at distal dendritic regions after SR, SO, and SLM stimulation.

1. Introduction

Neurons possess highly organized membrane structures through which membrane potential fluctuations play an important role in the integration of neural information. The integration properties of a neuron largely depend on neuronal channel properties and geometries. Many electrophysiological methods can directly access the electrical properties of dendrites (Stuart et al., 1993; Davie et al., 2006), even those of fine basal dendrites (Nevian et al., 2007). However, the actual degree of activation of excitatory and especially of inhibitory synapses terminating on a cell in on-going neuronal circuit activity is not clear.

The existence of inhibitory postsynaptic potentials elicited by stimulating the main input to the CA1 circuit has been long known (Kandel et al., 1961; Andersen et al., 1963, 1964; Buzsaki, 1984). This circuit has been designated as a recurrent inhibitory system. Feed-forward inhibition activated by orthodromic stimulation has also been identified (Dingledine and Gjerstad, 1980; Alger and Nicoll, 1982b). The locus of inhibitory synaptic input has been tested by local application of GABA in combination with local electrical stimulation (Andersen et al., 1980; Alger and Nicoll, 1982a), and the time course of the inhibitory input has been shown to overlap with the excitatory input (Dingledine and Langmoen, 1980; Brown and Johnston, 1983; Griffith et al., 1986; Turner, 1990; Karnup and Stelzer, 1999). Inhibition largely depends on shunting control and scarcely appears in the membrane potential trace (Turner, 1988; Sayer et al., 1989; Pouille and Scanziani, 2004). Thus, it has been difficult to measure the impact of inhibitory input

* Corresponding author at: Kagawa School of Pharmaceutical Sciences, Tokushima Bunri University, 1314-1 Shido, Sanuki, Kagawa 769-2193, Japan.
Tel.: +81 87 894 5111x6708; fax: +81 87 894 0181.
E-mail address: tominagat@kph.bunri-u.ac.jp (T. Tominaga).
[1] Present address: BrainVision Inc., 3-46-8 Narimasu, Itabashi, Tokyo 175-0094, Japan.

0168-0102/$ – see front matter
doi:10.1016/j.neures.2009.02.007

on the membrane potential response, especially in terms of its distribution along the somatodendritic axis of a cell. Since optical recording methods can visualize population behaviors within the CA1 circuit, we used this method to map the distribution of $GABA_A$ receptor-mediated inhibition along the somatodendritic axis of CA1 pyramidal cells (Megias et al., 2001) and to determine to what extent inhibition contributes to CA1 signal transduction.

The optical imaging method with voltage-sensitive dyes (VSDs) represents a potentially useful tool for examining integration processes (e.g., Antic and Zecevic, 1995; Antic, 2003). Because of its simple lamellar organization (Andersen et al., 1969b), the in vitro hippocampal slice preparation is ideal for studying neural integration in neural circuits. Optical imaging with VSDs has many advantages (Grinvald et al., 1982; Barish et al., 1996; Tominaga et al., 2000, 2001, 2002; Inoue et al., 2001; Mochida et al., 2001; Aihara et al., 2005; Mann et al., 2005a; Chang and Jackson, 2006): It allows direct viewing of hippocampal layers, thus allowing optical signals to be attributed to specific membrane areas of the major cell type, the pyramidal cell. For example, neural integration in area CA1 can be assessed by examining signals in stratum radiatum (SR), which correspond primarily to the membrane potential responses of pyramidal cell apical dendrites, and signals in stratum pyramidale (SP), which correspond primarily to membrane potential responses of pyramidal cell somas.

One potential drawback of optical recording, however, is that the nature of optical signals precludes an interpretation of the optical data in terms of absolute membrane potentials. A typical example is seen in optical signals resulting from stimulation of Schaffer collateral axons in SR. Even if the stimulus intensity is high enough to obtain saturated population spikes, the optical signals measured from SR (which correspond to a few tens of millivolts of excitatory postsynaptic potential [EPSP]), are larger than those measured from SP (which correspond to over a hundred millivolts of action potential). To identify the potential source of this disparity, we analyzed steady membrane potential changes in slices perfused with high-potassium medium, and examined the profiles of population membrane potential responses using a simulator called NEURON (Hines and Carnevale, 1997). The results suggest that the nature of the population optical signal is the major cause of the disparity.

Taking advantage of this optical measurement method, we have successfully characterized the inhibitory action and its distribution on actual membrane potential response of feed-forward and feedback inhibition within Schaffer collateral inputs to the perisomatic region of CA1 pyramidal cells and found that the spatial contribution of inhibitory inputs onto postsynaptic cells differed.

Some preliminary results of this study have been published in abstract form (Tominaga et al., 2003).

2. Materials and methods

All animal experiments were performed according to protocols approved by the Animal Care and Use Committee of Tokushima Bunri University and RIKEN, and the U.S. National Institutes of Health Guide for the Care and Use of Laboratory Animals. All efforts were made to minimize the number of animals used and their suffering.

2.1. Slice preparation and staining with VSD

Hippocampal slices (400 μm thick) were prepared from 4- to 5-week-old male rats, decapitated under deep-ether anesthesia. The brains were quickly cooled in ice-cold artificial cerebrospinal fluid (aCSF) (124 mM NaCl, 2.5 mM KCl, 2 mM $CaCl_2$, 2 mM $MgSO_4$, 1.25 mM NaH_2PO_4, 26 mM $NaHCO_3$, and 10 mM glucose, pH 7.4) bubbled with 95%/5% O_2/CO_2 gas. After cooling for 5 min, the hippocampus was dissected out along with the surrounding cortex and sliced into 400-μm-thick transverse sections with a vibratome (Leica VT-1000). Following a short incubation in gassed aCSF for 3–5 min, each slice was transferred onto a fine-mesh membrane filter (Omni Pore membrane filter, JHWP01300; Millipore Corp., MA, USA), held in place by a thin Plexiglas ring (inner diameter, 11 mm; outer diameter, 15 mm; thickness 1–2 mm). These slices were transferred to a moist chamber continuously supplied with the humidified O_2 and CO_2 gas mixture. The temperature was held at 32 8C for 1 h, and then maintained at room temperature. After 1 h of incubation, slices were stained with VSD (100 ml of staining solution/slice) for 25 min and washed with normal aCSF. VSD (0.2 mM Di-4-ANEPPS; D-1199, Molecular Probes Inc., OR, USA) was dissolved in a mixture of 2.7% ethanol, 0.13% Cremophor EL (Sigma), 50% fetal bovine serum (Sigma), and 50% aCSF. The slices were subjected to experiments after at least 1 h incubation at room temperature after the wash.

2.2. Optical recording

The Plexiglas ring supporting an individual slice was placed in an immersion-type recording chamber. Slices were continuously perfused with prewarmed (31 8C) and oxygenated (95%/5% O_2/CO_2 gas mixture) aCSF at a rate of 1 ml/min. Custom laboratory-designed epifluorescence optics consisting of two principal lenses was used. The optics consisting of a modified 35-mm camera lens (f = 50 mm F/1.4, Nikon; the final magnification of the system was • 1.5) or a custom made objective lens (Olympus MYCAM 5• /0.6 WI; the final magnification of the system was about • 5) as the objective lens, and a lens (f = 55 mm • 1.0 Leica Microsystems MZ-APO) as the projection lens. The excitation light was provided by a halogen lamp source (150 W; MHW-G150LR, Moritex Corp.) through a excitation filter (l = 530 • 10 nm) and reflected onto a specimen by a dichroic mirror (l = 575 nm). Fluorescence was passed through an emission filter (l > 590 nm) and projected onto a CCD camera or a MOS imager (MiCAM01 and MiCAM Ultima, respectively; BrainVision, Inc., Tokyo, Japan). Optical signals were calculated as the ratio of fractional change in VSD fluorescence to baseline VSD fluorescence (DF/F). The optical signals referred to in the following sections represent signals filtered in spatial and temporal dimensions with a Gaussian kernel of 5 • 5 • 3 (horizontal • vertical • temporal). We confirmed that this procedure produced steady and flat baselines and did not cause any artificial drift in signals in the absence of electrical stimulation. We analyzed the optical signals offline using a procedure developed for Igor Pro (WaveMetrics Inc., OR, USA). VSD fluorescence at a wavelength of 530 nm decreases in response to the depolarization of the membrane. To fit the polarity of the response to conventional membrane potential changes, we expressed the optical signal in a polarity that matches the membrane potential change. For example, decreased fluorescence, which corresponds to depolarization, is represented as a positive deflection. However, when a global fluorescence change was observed, we used the polarity of the fluorescence change, as shown in Fig. 2.

2.3. Time-lapse imaging

Since the imaging system was created and optimized for fast acquisition, slow changes in fluorescence, such as responses to bath application of test solutions, could not be evaluated. Accumulation of static charges on pixels of the imager over long periods tended to create unstable drifts in the baseline. To mitigate this problem, we acquired 85 consecutive frames of data at short intervals (85 frames at rate of 1 ms/frame), every 10 s. The

consecutive images captured during each frame were averaged, and this average represented frame data for each 10 s interval. A sequence of frames was produced using a macro developed for use in the MiCAM01 image acquisition program. These sequences were then analyzed using a laboratory-designed function of IgorPro (both macro and function available upon request).

2.4. Electrophysiological recording

Patch-clamp recordings in the whole-cell mode were made using a patch-clamp amplifier with a capacitive headstage (Axoclamp 700B, Axon Instruments, Foster City, CA) using pipettes (3–5 M) of borosilicate glass (Sutter Instruments, Novato, CA) pulled using a P-97 Flaming–Brown pipette puller (Sutter Instruments, Novato, CA). Whole-cell recordings were low-pass-filtered at 3 kHz and digitized at 10 kHz. Data were digitized with a digitizer (ITC-18, Instrutech Inc., NY) and fed into a computer for off-line analysis (Apple Computer) using a laboratory arranged software on IgorPro (WaveMetrics Inc., OR, USA). Electrical stimulation were applied by constant current pulses (A395, WPI) through a glass microcapillary tube (5 mm inner diameter; filled with aCSF) placed in the stratum oriens (SO), stratum radiatum and stratum lacunosum-moleculare (SLM). Neurons were visualized by the oblique illumination with aid of contrast enhancement of a CMOS-camera (SKDCE-2EX, Sigma Koki Co., Tokyo, Japan) with an upright microscope (BX-51WI, Olympus Tokyo, Japan). In voltage-clamp mode, a test membrane potential step (• 10 mV) were always applied prior to electrical stimulation, and traces with those series resistance (Rs) lower than 20 MV were accepted.

The pipette solution consisted of, in mM: 130 Cs-$MeSO_3$, 10 Hepes, 4 $MgCl_2$, 4 NaATP, 0.4 NaGTP, 10 Na-Phosphocreatine, 10 EGTA; PH was adjusted to 7.2. 5 mM QX-314 was also added.

A glass microcapillary tube (5 mm inner diameter; filled with aCSF) was used as a recording electrode for field potential recordings.

The electrophysiological recording system was controlled by a procedure developed in Igor Pro (WaveMetrics Inc., OR, USA).

2.5. Neuron simulation

Numerical simulations were performed with NEURON (ver. 5.7) (Hines and Carnevale, 1997) on a Macintosh computer (Mac OSX). A realistic morphological and electrophysiological multi-compartment model of a CA1 pyramidal neuron was employed (Migliore et al., 1999; Migliore, 2003). The model consisted of 202 compartments representing the neuron's axon, soma, and dendrites. Please refer to the Neuron Model DB (http://senselab.med.yale.edu/modeldb/ShowModel.asp?model=19696) for the detail of the distribution and kinetics of the active conductance (g_{Na}, g_{KDR}, g_{KA} and g_h), and passive electrical properties of the components and synaptic connections embedded into the model. The simulated membrane potential response of each compartment was analyzed, and membrane potential profiles were drawn using IgorPro software and custom-made macros.

We calculated two different membrane potential profiles. In order to obtain two different membrane potential profiles for the case where the cell produces almost same amplitude of EPSP while one with action potential and the other without, we changed weight value in the model to seek the threshold. The resulted membrane potential profiles obtained just below the threshold (weight was 1.231 e^{-2}, see Fig. 4Ba) and above the threshold (weight was 1.24 e^{-2}, see Fig. 4Bb) showed almost similar amplitude and time course of EPSP (Fig. 4A).

The membrane potential profile of a population of cells (Fig. 4C) was calculated as an average of membrane potential (Vm_{avg}) as function of distance from the soma (L) and proportion of the number of the non-excited cell relative to the excited cell (p) according to the equation below;

$$\frac{Vm_{avg}\cdot L;\ p\cdot\ \cdot\ \cdot p\cdot\ 1\cdot Vm_{epsp}\cdot L\cdot\ \cdot\ Vm_{AP}\cdot L\cdot\cdot}{p} \quad (1)$$

where $Vm_{epsp}(L)$ and $Vm_{AP}(L)$ are the membrane potential caused by the just below the threshold and just above the threshold, corresponding to the membrane potential profiles drawn in Fig. 4Ba and Bb respectively.

The PR ratio in Fig. 4D was calculated the ratio of the responses in SP (L = 0 mm) and those in SR (L = 250 mm), as a function of the proportion (p);

$$\text{PR ratio}\cdot p\cdot\ \cdot\ \frac{Vm_{avg}\cdot 0;\ p\cdot}{Vm_{avg}\cdot 250;\ p\cdot} \quad (2)$$

The PR ratio for optical signal was calculated as the ratio of the amplitude of optical signal at L = 0 mm and those at L = 250 mm.

3. Results

3.1. Amplitude distribution of neuronal responses in the optical signal

VSDs are molecular probes that convert membrane potential changes to changes in fluorescence. Fig. 1B–D shows a typical optical signal response when an electrical stimulus (250 mA, 200 ms in positive–negative direction) is applied to the Schaffer collaterals in area CA1 of the hippocampus (please see Tominaga et al., 2000, 2002).

Fig. 1B shows consecutive images of optical signals obtained at different times, starting from the stimulation. Representative traces of responses as a function of time, recorded at representative pixels are presented in the lower part of the panel. The left-most trace shows responses recorded at the stimulating site, showing that the stimulus artifact was followed by the postsynaptic response. The large arrow in this trace points to the peak of the stimulus artifact. Representative traces recorded from mid- and distal parts of CA1 are also indicated by large arrows. Because the peaks of individual optical traces appeared at different times due to propagation of the response, we used the peak amplitude as representative values in the following section to compare the amplitude of the response.

The time course of the optical signal along the somatodendritic axis of pyramidal cells is shown in Fig. 1C. The largest change appeared in the middle of SR, while in SP the peak was smaller and was followed by a hyperpolarizing response. The traces at each representative pixel are shown in Fig. 1D. Traces corresponding to different stimulus intensities are shown in pseudo-color code. Regardless of stimulus intensity, in SR responses were larger than those in other layers, whereas in SP responses were smaller, but hyperpolarizing responses were larger than those in other layers.

The distribution of the amplitude information was mapped (projected) onto a single frame in Fig. 1E, which shows the amplitude distribution of the maximum response (traces with arrows in Fig. 1B) at each pixel (maximum response map). Profiles of the maximum amplitude map along the somatodendritic axis of pyramidal cells are shown in Fig. 1F. The response profiles at different distances from the stimulating site (90, 180, 360, 540 mm) are shown. At each site, the peak response appeared in the middle of the SR (about 200 mm from the soma). The maximum response measured in stratum oriens was 70% or less of that measured in SR. This relationship was maintained across stimulus intensities (Fig. 1G and H); at each stimulus intensity, the peak amplitude of the optical signal was larger in SR.

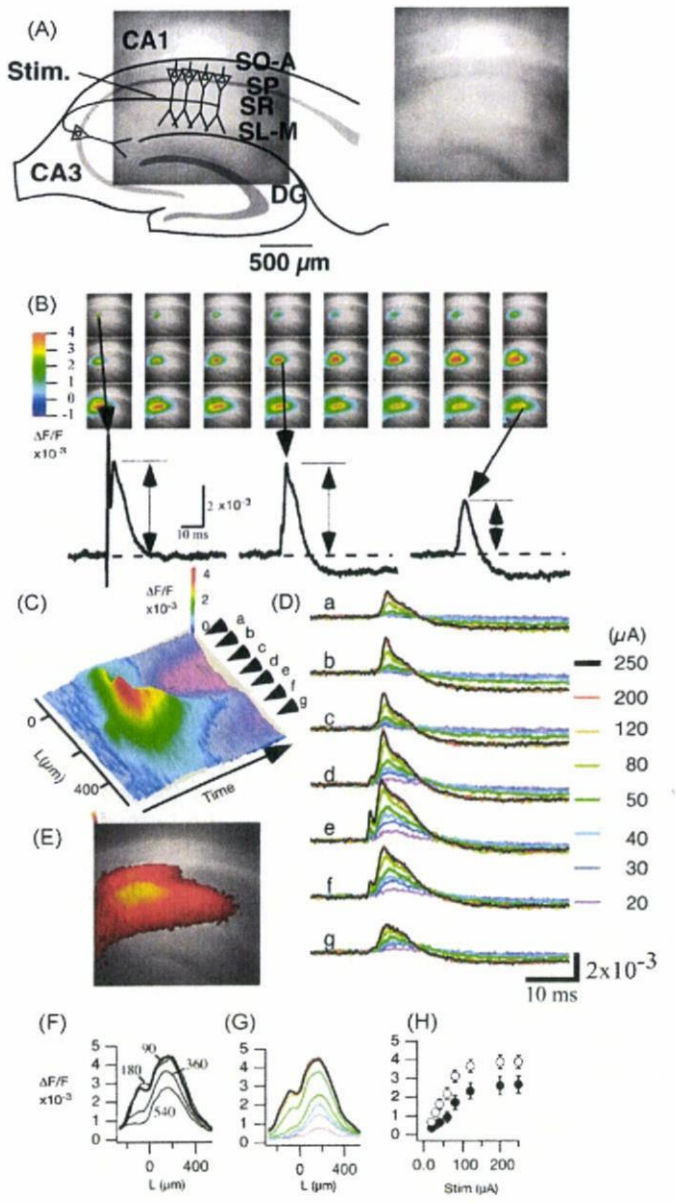

Fig. 1. Amplitude distribution of a Schaffer-collateral-evoked optical signal in area CA1 in the rat hippocampal slice preparation. (A) Schematic illustration of a rat hippocampal slice superimposed onto the fluorescent image of the recording area. The sampled area of the imaging system was about 1.8 mm • 1.8 mm. Stim., stimulation electrode; SO-A, stratum oriens-alveus; SP, stratum pyramidale; SR, stratum radiatum; SLM, stratum lacunosum-moleculare. (B) Consecutive images (left to right, top to bottom) showing optical signals obtained every 0.2 ms, starting from the stimulation. Lower traces are representative traces obtained at pixels in the indicated field of view. Arrows show the pixel where the signal showed a peak in the consecutive images. (C) A pseudo-colored three-dimensional graph of a slit recording of the optical signal in B obtained at about 90 mm from the stimulating electrode. (D) The representative traces of the optical signals recorded from representative pixels a–g in the slit image shown in panel C. The pseudo-color coded traces in a–g represent responses to different stimulus intensities (20, 30, 40, 50, 80, 120, 200, 250 mA, respectively). (E) A pseudo-colored image of the projection of the maximum response at each pixel. (F) Maximum response profiles of the slice image in C (thick trace) and at slits at increasing distances (180, 360, 540 mm) from the stimulating electrode. (G) Response profiles at 90 mm from the stimulating electrode at different stimulus intensities. These color coded responses correspond to those shown in panel D. (H) Stimulus–response relationships recorded from SR (open circles, 200 mm from the soma) and SP (filled circles) (n = 6 slices; bars, SEM). The data were acquired with a MiCAM ultima system sampling at a 10 kHz frame rate.

The soma responses should correspond to action potential firing in the pyramidal cell layer and should be over 100 mV of the membrane potential shift, while dendritic responses in SR should correspond to EPSPs and should be a few tens of millivolts of the membrane potential shift. If the response measured by VSD reflects the membrane potential amplitude, then we would expect larger responses in SP than in SR. In our optical recordings, however, we observed the opposite: Optical signals in SR were larger than those in SP. This observation raises the possibility that the VSD signal varies in sensitivity to membrane potential changes in different layers. If this were indeed the case, then it would be difficult to use VSD signals to compare the membrane potential response along the somatodendritic axis of pyramidal cells.

3.2. Changes in fluorescence caused by steady resting membrane depolarization show less VSD-signal-layer specificity

The apparent lack of correspondence between the amplitudes of the optical signal and actual membrane potential changes in SP and SR could be due to (1) tissue-dependent differences in VSD sensitivity, or (2) the population nature of the optical signal. To test these possibilities, we visualized steady fluorescence changes in response to experimental manipulation of $[K^+]_O$, which should cause tissue-independent, uniform depolarization of the resting membrane.

Switching the perfusate from control aCSF ($[K^+]_O$ = 2.5 mM) to a high-K^+ solution ($[K^+]_O$ = 25 mM) produced decreased fluorescence (Fig. 2A). Washing out the high-K^+ solution caused the responses to recover, with fluorescence levels returning to control levels. The distribution of the depolarizing response, as measured by a decrease in fluorescence, is shown in Fig. 2Ba. The ratio of the decrease relative to initial fluorescence (Fig. 2Ba) shows uniform changes in fluorescence in SR, while large changes occur in SP and SO (yellow-orange peaks orthogonal to the blue plane, Fig. 2B, panel a; also see Fig. 2C).

To test whether the large fluorescence change in SP and SO was caused by action potentials arising from postsynaptic cells, we added TTX to the high-K^+ perfusate (Fig. 2Bb). The steep peak disappeared when TTX was added to the high-K^+ solution (Fig. 2B, panel b). Profiles of the fluorescence changes along the somato-dendritic axis of pyramidal cells are plotted in the graph of Fig. 2C and pooled data are plotted in the graph of Fig. 2D. These profiles show that the high-K^+-associated (open circles) peak responses detected in SP and SO were greatly diminished by the application of TTX (filled circles). At each sampling point along the entire length of layers, the difference between pre-TTX and post-TTX was $p < 0.05$. This suggested that the peak was caused by action potential firing of neurons.

To exclude the effects of transmitter release from depolarized cells, we applied a cocktail containing major excitatory and inhibitory receptor blockers (50 mM APV, 10 mM CNQX, 20 mM bicuculline) to the high-K^+ perfusate (open triangles). The cocktail reduced the high-K^+-depolarizing response ($p < 0.05$) in SR, SO, and stratum lacunosum-moleculare (SLM), suggesting that excess glutamate and/or GABA around the cells contributed in part to the depolarization we observed in slices bathed in high-K^+ solution. A peak near the soma region was abolished with TTX (filled triangles). Hence, this observation supports the possibility that the unequal distribution of fluorescence change in SP was caused mostly by action potentials from postsynaptic cells.

The steady and uniform fluorescence changes we observed in the absence of action potential (in TTX) imply that differences in layer-dependent VSD sensitivity may not be a major cause of the apparent mismatch between the optical signal amplitude and membrane potential response amplitude shown in Fig. 1.

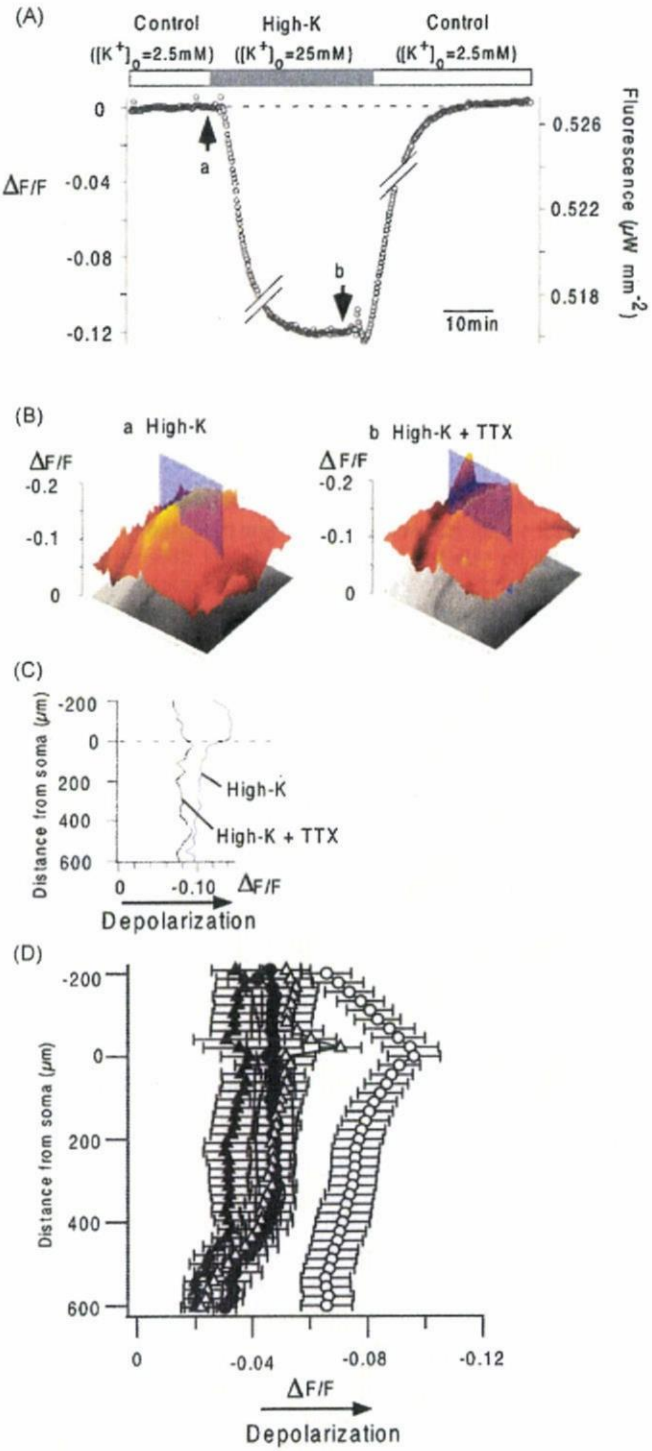

Fig. 2. Changes in VSD fluorescence measured in the middle of the SR of area CA1. (A) Relative fluorescence intensity (DF/F) was measured and plotted against time. Each dot represents the average of 85 frames of fluorescent images obtained at a rate of 1 ms/frame and at 10 s intervals. The external solution was changed to a higher K^+ solution ($[K^+]_O$ = 25 mM) from normal aCSF ($[K^+]_O$ = 2.5 mM) for 30 min. The absolute fluorescence intensity is indicated in the right axis. Arrows labeled a and b point to the representative frames used for constructing the graphs in panel B. (B) The effect of TTX on the distribution of fluorescence changes in response to stimulation with high-K^+ solution. Three-dimensional graphs showing the amplitude of responses to high-K^+ solution in the absence (a) and presence (b) of TTX. TTX decreased the amplitude of responses, as reflected by a decrease in fluorescence. (C) Profiles of fluorescence changes along the somatodendritic axis of pyramidal cells in the absence (high-K^+) and presence of TTX (high-K^+ + TTX). (D) Pooled data of fluorescence changes under high-K^+ (open circles) and high-K^+ + TTX (filled circles) conditions. The other set of data show the changes after application of APV, CNQX, and bicuculline without TTX (open triangles) and with TTX (filled triangles). Data are means • SEMs (n = 4–9 slices).

3.3. The distribution of membrane potential responses along the somatodendritic axis of pyramidal cells as simulated with the NEURON simulator was similar to the membrane potential profiles measured in slices bathed in high-K^+ solution

The population nature of the optical signal may underlie the apparent mismatch between the optical signal amplitude and membrane potential response amplitude. To test whether this is the case, we changed the composition of a population of cells so that it comprised cells that fire action potentials and those that do not when stimulated by a single electrical shock to the Schaffer collaterals. Since it is difficult to identify these cells and alter the population of cells accordingly, we used a realistic numerical model of a hippocampal CA1 pyramidal neuron (Migliore et al., 1999) to simulate the distribution of membrane potential responses in area CA1. The software we used is called NEURON (Hines and Carnevale, 1997). Fig. 3A illustrates this model in terms of a tree-like drawing showing the topographical geometry of the CA1 pyramidal neuron we modeled. The traces in Fig. 3A show representative membrane potential responses at different sites (0, 100, 200, and 300 mm from the soma) in response to a relatively strong synaptic input. The membrane potential responses in different segments were used to estimate the distribution of the response along the somatodendritic axis of the cell using information about the digital morphological reconstructions of the cell.

Fig. 3B shows the membrane potential response profiles along the somatodendritic axis of the CA1 pyramidal neuron we calculated using the simulation results when either a just-above threshold or a just-below threshold input was provided. In this model, the synapses terminated 200 mm from the soma. Thus, we could reproduce the membrane potential profiles of cells that fire action potentials (Fig. 3Ba) and of those that do not fire action potentials (Fig. 3Bb) but have almost identical EPSP amplitudes.

The membrane potential responses along the somatodendritic axis of the pyramidal cell are shown in the three-dimensional (3D) graphs of Fig. 3B. Although the size of the EPSP was almost identical, the overall potential profiles were quite different. When the pyramidal cell fired an action potential, very strong responses (almost 80 mV) occurred in SP and SO, and rather small (40 mV) responses occurred in the middle part of the apical dendrite (L = 300 mm) (Fig. 3Ba). On the other hand, when the pyramidal cell did not fire an action potential, small responses occurred in the middle part of the dendrite (Fig. 3Bb). Both of these simulations did not resemble the amplitude and distribution of responses we obtained by optical recording (cf. Fig. 1).

3.4. Reducing the proportion of excited neurons can mimic the profile of responses obtained by the optical recording method

Fig. 4 shows membrane potential response profiles calculated from our simulated results. We simulated membrane potential responses to apical dendritic synaptic input that was just below threshold for action potential generation (EPSP only; gray trace in Fig. 4A) and to synaptic input that was just above threshold (EPSP followed by an action potential; black trace in Fig. 4A). The distribution of peak membrane potential changes along the somatodendritic axis of the modeled pyramidal neuron is shown in Fig. 4B (panels a and b, respectively). It is clear from the figure that the shapes of the two membrane potential profiles are quite different. When the pyramidal cell received just-above threshold input that elicited an action potential, the membrane potential responses over SP (distance < 0 mm from the soma) showed a large plateau; the tail-end of the response at the apical dendrite showed no obvious peak (Fig. 4B, panel b). On the other hand, when the pyramidal cell received just-below threshold input that failed to

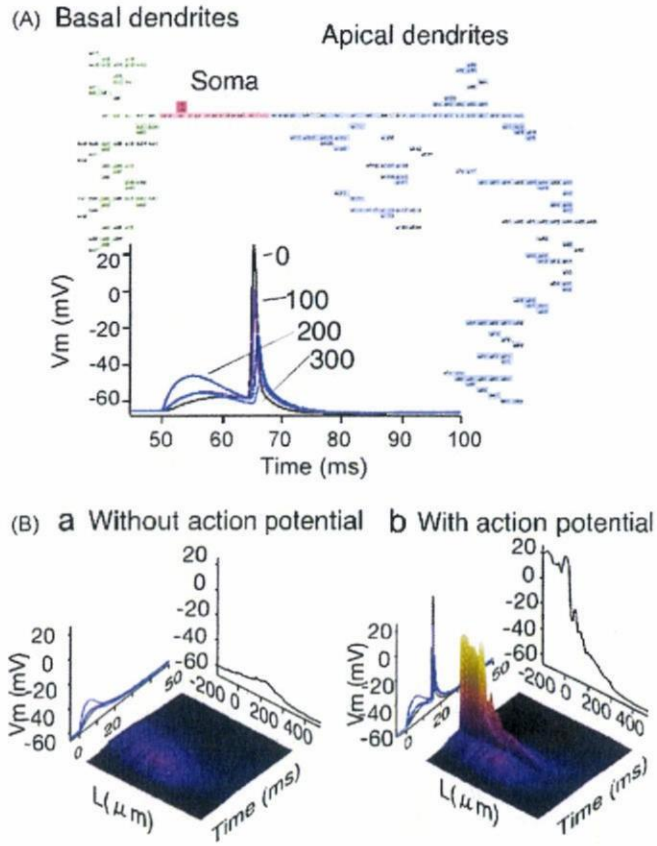

Fig. 3. (A) A realistic multi-compartment model of a pyramidal cell. Each segment has its own electrophysiological characteristics. The graph shows membrane potential responses of different segments located at different distances from the soma. The membrane potential responses were calculated from our model using the NEURON simulator program (Hines and Carnevale, 1997). (B) Time course of representative profiles of membrane potential changes along the somatodendritic axis of a CA1 pyramidal neuron in response to a weak synaptic input that fails to cause an action potential at the soma (a) and to a strong synaptic input that causes an action potential at the soma (b). These profiles were calculated by averaging the membrane potential responses measured from each compartment of the neuron model. Each 3D graph contains linear plots showing the kinetics of membrane potential changes (left) and the peak membrane potential profiles (right).

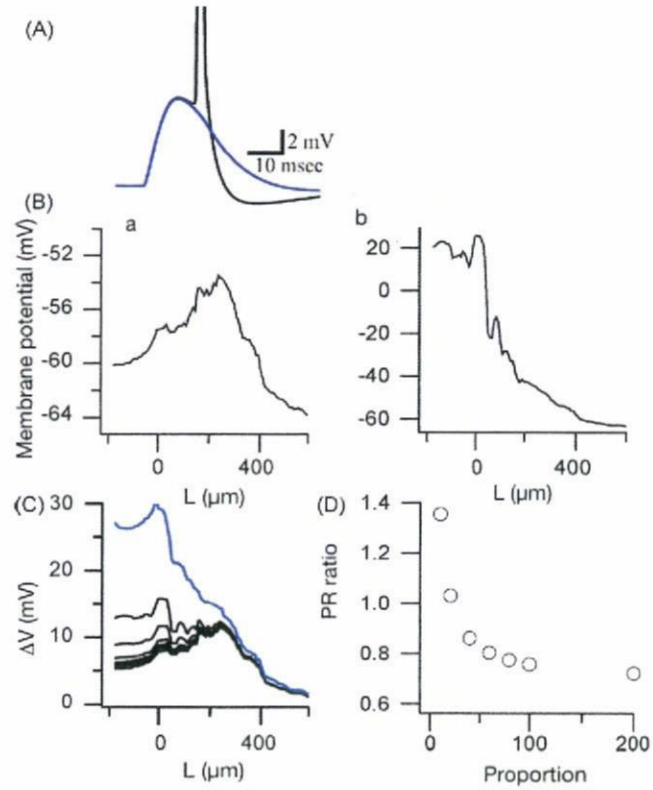

Fig. 4. Profiles of membrane potential responses to simulated synaptic input. (A) Traces representing membrane potential changes at the soma, as simulated using NEURON. The black trace represents responses to a just-above threshold synaptic input; the blue trace represents responses to a just-below threshold input. (B) Membrane potential profiles along the somatodendritic axis of the modeled pyramidal cell when it received just-below threshold input (a) and just-above threshold input (b). (C) Black traces show average membrane potential profiles of a modeled pyramidal cell when the network comprised different proportions of excited and non-excited cells (1:10, 1:20, 1:40, 1:60, 1:80, 1:100, 1:200), i.e., a neuron that fired an action potential (Ba) or one that did not fire an action potential (Bb). A blue trace show membrane potential profile when the action potential firing show random jitter within a range of 16 ms. (D) Changes in the PR ratio, the ratio of membrane potential responses in SP (soma; L = 0 μm) relative to those in SR (dendrites; L = 250 μm), caused by changing the proportion of excited cells and non-excited cells. See Section 2 for detail.

elicit an action potential, the membrane responses at the middle of SR (distance = 250 μm) showed a small peak (Fig. 4B, panel a). The model employed here is a realistic model neuron that had "active" apical dendrites (Magee and Johnston, 1995; Migliore et al., 1999; Johnston et al., 2003). For the input condition that produced an action potential, the ratio of the membrane potential amplitude in SP to that in SR was 5.13, whereas for the input condition that failed to produce an action potential, this ratio was 0.63. That is, the response was five times larger in SP than in SR when the cell generated an action potential. When the cell generated only an EPSP (Fig. 4Ba), the response in SP was smaller than that in SR.

Fig. 4C shows the profiles of averaged responses when the number of the cells was changed to contain fewer excited neurons (i.e., neurons that generated action potentials; Fig. 4Bb) relative to non-excited neurons (i.e., neurons that generated only EPSPs; Fig. 4Ba) (see Section 2). The shape of the membrane potential profile in Fig. 4C resembled the shape of the membrane potential profile reflected in the optical signal (Figs. 1F,G and 5B). On the other hand, changing the timing of the action potential firing within the range of 16 ms randomly did not affect the shape of the profile much (Fig. 4C blue). Fig. 4D shows the PR ratio, the ratio of the responses in SP (L = 0 μm) and those in SR (L = 250 μm), as a function of different excited cell-to-non-excited cell proportions (p; see Section 2). The PR ratio decreased as we reduced the proportion of excited cells to non-excited cells. When the model comprised one exited cell among 10 cells, the PR ratio was 1.35. However, when the model comprised one excited cell among 200 cells, the PR ratio decreased to 0.72. We chose the latter model to contain 200 cells because this is the maximum number of cells viewable with our imaging system, which covers an area of about 25 μm • 25 μm at the objective plane. The number of cells, therefore, covered by a single pixel should not exceed 200 cells, assuming that the diameter of a cell is 10 μm and the optical signal covers a depth of 200 μm (de Curtis et al., 1999).

For the optical signal shown in Fig. 1E, the PR ratio was about 0.73, which was higher than PR ratios calculated in our simulations and higher than PR ratios calculated from pooled optical recording data (0.67 • 0.07, mean • SEM; n = 6 slices; Fig. 5C, open circles). The PR ratio was calculated as a ratio of the ratio of the amplitude of optical signal at soma layer (L = 0 μm) and those at middle of SR (L = 250 μm). Fig. 5C (open circles) shows the PR ratios from pooled data as a function of stimulus intensity. The PR ratio first decreased as stimulus intensity increased, then increased, reaching a maximum of 0.7. The decrement of the PR ratio at lower stimulus intensities suggests that the membrane potential profile might reflect feed-forward inhibition activated by Schaffer collateral stimulation (Alger and Nicoll, 1982b; Turner, 1990).

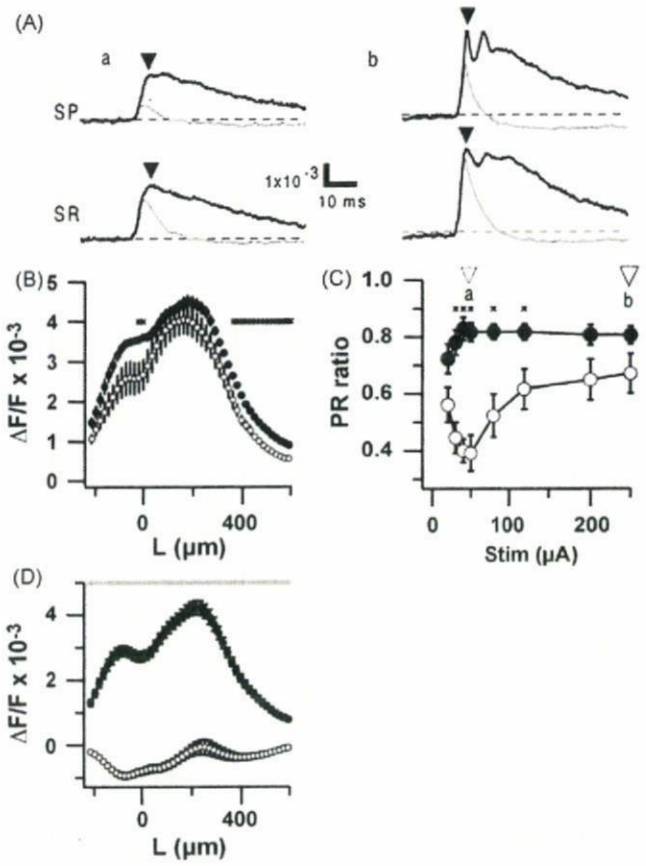

Fig. 5. (A) Time course of optical signals recorded from slices bathed in normal aCSF and after application of PITX. Responses to a weak stimulus (50 mA) (a) and responses to a strong stimulus (250 mA) (b) are shown. Black traces show the time course in the presence of PITX; gray traces represent controls. SP, traces obtained at a pixel corresponding to SP; SR, traces obtained at a pixel in the middle of SR. (B) Membrane potential profiles obtained from pooled optical recording data. The membrane potential responses were recorded 90 mm from the stimulating site. Open circles, slices bathed with normal aCSF (control); filled circles, slices treated with 100 mM PITX. (C) Changes in the PR ratio of optical signal as a function of stimulus intensity (n = 6 slices; error bars, SEM). Open circles, slices bathed with normal aCSF (control); filled circles, slices treated with 100 mM PITX. Open arrowheads (a and b) show the stimulus intensities corresponding to traces in panel A. (D) Membrane potential profile 25–30 ms following stimulation of control (open circles) and 100 mM PITX-treated (filled circles) slices. Asterisks on traces (B, C, D) indicate significant differences between profiles recorded under control and PITX treatment conditions (ANOVA, $P < 0.05$).

3.5. Optical signals revealed the impact of feed-forward inhibition on signal propagation in the area CA1 circuit in response to SR stimulation

The firing of principal neurons in area CA1 are thought to be under the control of feed-forward inhibitory inputs in addition to feedback types of control in the circuit (Buzsaki, 1984). In feed-forward inhibition the amount of inhibition is not controlled by the activation of postsynaptic principal neurons. To determine how inhibitory inputs affect membrane potential changes along the somatodendritic axis of a pyramidal cell upon SR stimulation, we applied PITX, a $GABA_A$ receptor inhibitor, to the aCSF solution bathing the hippocampal slices and monitored optical signals in SP and SR of area CA1 (Fig. 5).

The effect of PITX on the optical signal is shown in Fig. 5A. PITX increased the amplitude of the optical signals and prolonged the response. We defined the increase in the first peak of the response (filled arrowheads in Fig. 5A) caused by PITX application as feed-forward inhibition, because this increase preceded the action potential firing of the postsynaptic cells (see also Fig. 1D). The effect of feed-forward inhibitory inputs along the somatodendritic axis is also shown in Fig. 5B as membrane potential profiles of the first peak, in which the application of PITX increased responses significantly in the perisomatic region (• 20 mm < L < 0 mm) and distal apical dendritic region (L > 360.1 mm) (ANOVA, $p < 0.05$). Responses in SR, however, remained almost the same as in the control condition.

To show control over action potential firing, we plotted PR ratios (Fig. 5C). The initial decrease in PR ratio was abolished by adding 100 mM PITX to the aCSF (Fig. 5C, filled circles). That is, as the EPSP increased, spike activation probability increased in the presence of PITX. For comparison with feed-forward inhibition phase, changes in the falling phase (30 ms after stimulation) of the response are shown in Fig. 5D. A hyperpolarizing response was seen in SO and on apical dendrites 400 mm from somatic and perisomatic regions. As is clear in the figure, the hyperpolarizing response was replaced with a depolarizing response that occurred along the entire length of the somatodendritic axis. This could mostly reflect the impact of feedback inhibition on pyramidal cell activity.

3.6. Optical signals revealed the impact of feed-forward inhibition on signal propagation in the area CA1 circuit in response to SLM and SO stimulation

To examine the amount feed-forward inhibitory control contributed by major input pathways, we assessed membrane potential profiles in response to SLM and SO stimulation (Fig. 6).

PITX application significantly enhanced the SLM stimulation-induced response in both perisomatic and distal apical dendritic regions, as was seen with SR stimulation (Fig. 6B). Significant differences (asterisks; $P < 0.05$) were also observed in SO and in perisomatic (• 200 mm < L < 126.2 mm) and distal apical dendritic regions (L > 381.3 mm). It is interesting to note that changes in the PR ratio after SLM stimulation (Fig. 6C) were quite different from changes in the PR ratio after SR stimulation (Fig. 5C), even though both reflect perisomatic inhibition (cf. Figs. 5B and 6B). Upon SLM stimulation, inhibition in the perisomatic region increased as stimulus intensity increased, as shown in Fig. 6C, and was significantly different ($P < 0.05$) at stimulus intensities greater than 120 mA. SO stimulation induced larger responses in SO and in somatic regions. Although PITX application failed to appreciably affect these responses, PITX affected responses recorded in distal dendrites, with significant differences observed in regions farther than 258.8 mm from the soma. This can also be seen in the PR ratio shown in Fig. 6G. After-hyperpolarization in the perisomatic region was clear and PITX treatment induced full-range depolarization along the somatodendritic axis.

3.7. Electrophysiological recording and stimulation

Fig. 7 shows the representative current responses of a pyramidal cell in the area CA1 upon the SR, SLM and SO stimulation at two different stimulus intensities (250 mA and 40 mA) at different holding potentials (• 90 mV to • 20 mV). Stimulation elicited a mixture of excitatory postsynaptic current (EPSC) and inhibitory postsynaptic current (IPSC). As is clear in the Fig. 7A SR stimulation most right-hand expanded traces at depolarized holding potential (• 30 mV), a weak stimulation (40 mA) caused only fast feed-forward IPSC following a sharp small inward EPSC, while increasing stimulation intensity to 250 mA additionally recruited following feedback IPSC (Glickfeld and Scanziani, 2006). This was not clear in SO stimulation and SLM stimulation (Fig. 7B SO and C SLM). The IPSC was not clearly seen on the traces at • 70 mV, since the calculated reversal potential for chloride ion (E_{Cl}) was about • 73 mV. All the cells tested (n = 6) showed similar tendency.

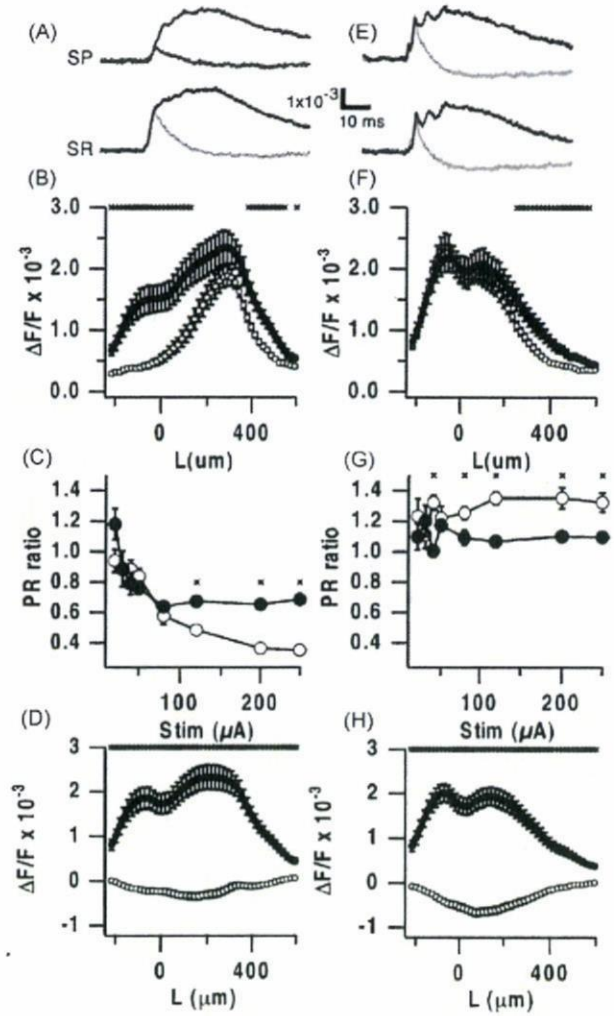

Fig. 6. (A, E) Time course of optical signals recorded from slices bathed in normal aCSF and after application of PITX following SLM stimulation (A) and SO stimulation (E). Black traces show the time course in the presence of PITX; gray traces represent controls. SP, traces obtained at a pixel corresponding to SP; SR, traces obtained at a pixel in the middle of SR. (B, F) Membrane potential profiles obtained from pooled optical recording data for SLM stimulation (B) and SO stimulation (F). The membrane potential responses were recorded 90 mm from the stimulating site. Open circles, slices bathed with normal aCSF (control); filled circles, slices treated with 100 mM PITX. (C, G) Changes in the PR ratio after SLM stimulation (C) and after SO stimulation (G) as a function of stimulus intensity (n = 7 slices; error bars, SEM). Open circles, slices bathed with normal aCSF (control); filled circles, slices treated with 100 mM PITX. (D, H) Membrane potential profiles 25–30 ms of control (open circles) and in 100 mM PITX-treated (filled circles) slices following SLM stimulation (D) and SO stimulation (H). These profiles were obtained from pooled optical recording data. Asterisks on traces (B, C, D, F, G, H) indicate significant differences between profiles recorded under control and PITX treatment conditions (ANOVA, $P < 0.05$).

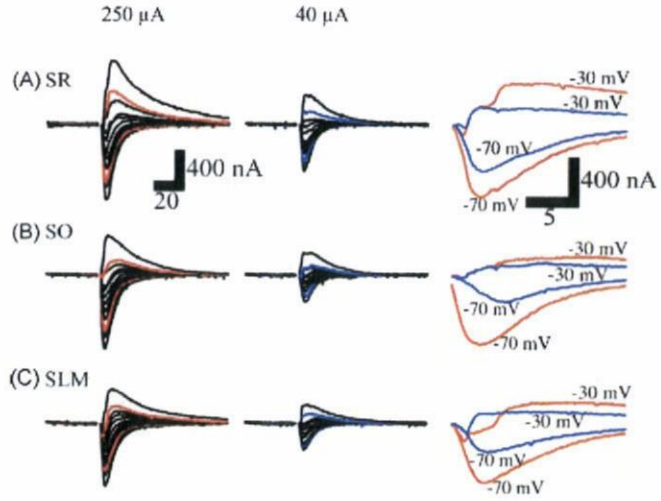

Fig. 7. Voltage-clamp recording from a pyramidal cell in response to SR stimulation (A), SO stimulation (B) and SLM stimulation (C) at two different stimulus intensities (250 mA; left column) and (40 mA; center column) at different holding potentials at • 80, • 75, • 70, • 65, • 60, • 55, • 50, • 45, • 40, • 35, • 30 and • 20 mV. The expanded and superimposed traces at right-most column show the current response at depolarized condition (• 30 mV) and near the resting membrane potential (• 70 mV) upon strong stimulus (250 mA; red) and weak stimulus (40 mA; blue). Stimulation was applied about 90 mm from the pyramidal cell under whole-cell clamp condition.

4. Discussion

In the present study, we have shown that optical recording with VSD can be used to measure membrane potential responses of pyramidal cells in area CA1 of the hippocampal slice after stimulating the Schaffer collateral pathway. This method allowed us to demonstrate the impact of a feed-forward inhibitory circuit on signal propagation following Schaffer collateral activation (Fig. 5). It is rather difficult to show the amount of neuronal activity affected by feed-forward inhibitory pathways because available methods are limited in their ability to detect neuronal activity sensitive to inhibitory actions (Turner, 1990).

The reduction of PR ratios (Fig. 5C) at lower stimulus intensities and the blockade of this reduction by PITX corresponds with observations that weak orthodromic stimuli can evoke IPSPs (Andersen et al., 1969a; Turner, 1988, 1990) and IPSC (see Fig. 7A). PITX-induced changes in the membrane potential profiles were mainly observed in SP, not SR (Fig. 5B). This might be caused by a change in the probability of action potential firing, as predicted by our simulation model (Fig. 4C). Much electrophysiological and anatomical evidence exists that shows feed-forward inhibition affects pyramidal cell excitability through inhibitory synaptic terminals in SP (Alger and Nicoll, 1982b; Buzsaki, 1984; Lacaille and Schwartzkroin, 1988a,b; Turner, 1990; Cobb et al., 1997; Megias et al., 2001). Feed-forward inhibition is thought to make possible the precise control of spike firing timing (Pouille and Scanziani, 2001, 2004). Our findings show that optical recording methods can allow us to visualize the degree of inhibition in an intact neuronal circuit, which is often difficult to access through traditional electrophysiological methods (Verheugen et al., 1999).

The inhibitory network in the hippocampus consists of many kinds of interneurons (Buhl et al., 1994; Freund and Buzsaki, 1996) and plays a crucial role in brain function, especially in memory formation and retrieval, by causing oscillations (Buzsáki, 2002; Mann and Paulsen, 2005, 2006). Oscillations depend on the time-dependent phasic regulation of unequally distributed excitatory and inhibitory inputs along the somatodendritic axis of a pyramidal cell (Megias et al., 2001) and act as "dipoles" (Buzsáki, 2002). The ability to measure somatodendritic membrane potential profiles with VSD-optical recording methods will be useful to reveal the dynamics of inhibitory networks (Mann et al., 2005b).

The SLM stimulation (Figs. 6B and 7B) elicited smaller optical response compared to that to SR stimulation (Fig. 5B). This may reflect the smaller temporoammonic pathway (TA pathway) fEPSP response to SLM stimulation (Remondes and Schuman, 2002, 2003), although our SLM stimulation may contain contamination of Schaffer collateral stimulation. Please note that the response caused by SO stimulation shown in Figs. 6E–H and 7C did not include fraction of the response caused by direct stimulation of pyramidal cells, since the response was not seen under the blockade of glutamergic synaptic connection. They are mostly

reflecting the back propagation of action potential firing of the pyramidal cells caused by synaptic transmission to the basal dendrite when the stimulus intensity was strong.

The stimulus–response relationships, as reflected in the PR ratios, following SR and SLM stimulation (Figs. 5C and 6C) were quite different. That is, the PITX effect reached maximum levels at lower stimulus intensities during SR stimulation (Fig. 5C), while the effect reached maximum levels at higher stimulus intensities during SLM stimulation (Fig. 6C). Since both modes of stimulation induced significant inhibition in the perisomatic region while sparing responses from the center of the apical dendrite, the differences in PR ratios may be due to differential control of feed-forward inhibition to the perisomatic region. The input pathways to CA1 vary such that SR receives inputs from CA3 whereas SLM receives inputs from entorhinal cortex. Thus, the differences we observed may be due to differences in synaptic action on the same class of interneurons (Kajiwara et al., 2008) or may reflect the recruitment of different classes of inhibitory interneurons. This difference may be due to differential control of CA1 pyramidal cell excitation, since SR receives inputs from CA3 whereas SLM receives inputs from entorhinal cortex. On the other hand, feed-forward inhibition was not observed in perisomatic regions after SO stimulation, even though it was detected in distal dendritic regions. This difference may be due to the fact that SO contains inputs from recurrent collaterals and to a lesser extent from Schaffer collaterals. The role of these different types of feed-forward inhibition in the CA1 network should be examined further in detail.

4.1. Does DF/F reflect the amount of membrane potential change in different membrane compartments?

Evaluating the size of optical signals has continued to be problematic, ever since VSD (WW-401) was first used for optical recording in mammalian brain slice preparations (Grinvald et al., 1982). Moreover, it was uncertain whether optical signal amplitude varied in different tissue components. DF/F is usually used to calibrate optical signals to some extent according to fluorescent dye (e.g., RH-796, RH-418, Di-4-ANEPPS, Di-8-ANEPPS). These measures are based on the observations that optical signals change proportionally according to membrane potential changes (Conti and Tasaki, 1970; Cohen et al., 1974; Ross et al., 1977) and that the proportionality constant of a single membrane or a single cell is the same. Evaluating the amplitude of an optical signal in tissues is more difficult because we cannot simply assume that fluorescence intensity actually reflects dye in the membranes in which we want to measure membrane potentials. We can classify a dye that has incorporated into neuronal tissue into three categories depending on where the dye is incorporated: (1) dyes that incorporate into neuronal membranes (active neuronal dye); (2) dyes that incorporate into glial membranes (active glial dye); and (3) dyes that incorporate into dead cells, connective tissues, and other lipids (inactive dye). The latter class of dyes should not show membrane potential changes. If we want to visualize fast neuronal responses via VSD signals, the second and third classes of dye should appear as offsets (F_{offset}). These offsets increase only the denominator of an optical signal, and thus decrease the dye's sensitivity to membrane potential changes, i.e., DF/F becomes smaller. In other words, even if the same membrane potential change occurs in neurons in a tissue, DF/F can vary depending on the characteristics of the tissue if F_{offset} is different.

When hippocampal slices were stimulated with a high-K^+ solution and treated with TTX, the changes in fluorescence were almost equal in different layers (Fig. 2D). This suggests that, at least in area CA1, the specificity of the dye for different layers (SO, SP, SR, SLM) is fairly similar. This implies that the second and third class of dyes behave similarly in different layers.

We do not know how the second class of dyes (glial dyes) affects optical signals, but it seems that how a dye affects optical signals largely depends on the dye itself. Non-fluorescent dyes, which are visualized through absorption changes at certain wavelengths (e.g., RH-155), have been reported to be more sensitive to glial membrane potential changes (Kojima et al., 1999; Kawamura et al., 2004). Unlike Kojima and colleagues, however, we observed almost no effect on optical signal time course in response to a glial transporter inhibitor (Tominaga et al., 2002). In addition, their optical signals often lacked hyperpolarizing signals that follow the EPSP-action potential response. On the other hand, using optical recording, we observed $GABA_A$ receptor antagonist-sensitive IPSPs that are observable in intracellular recordings (Figs. 1D and 5D and also see Fig. 5 in Tominaga et al., 2000). Thus, signals observed with RH-155 would not be detected by Di-4-ANEPPS, the fluorescent dye we used in the present study (Chang and Jackson, 2003).

4.2. The population nature of the optical signal

Our simulation results (Fig. 4) show that the optical signal may be influenced by the neuronal makeup of the network. In our neural network model of area CA1, we changed only the proportion of cells firing action potentials (excited cells) to those not producing action potentials (non-excited cells). The ratio of excited to non-excited cells needed to be reduced to 1:100 so that the membrane potential profile was similar to the optical signal. This big difference in the number of excited cells versus non-excited cells should decrease if we incorporate into the model randomness in the timing of action potentials. This should be examined in future experiments. In order to minimize introduction of assumptions on the population activity, we had to use extremely simplified binary population calculated with single NEURON model. This, in turn, could exclude some aspects of dendritic membrane potential dynamics (Golding and Spruston, 1998; Sjostrom et al., 2008). Although our simulation showed that the population nature could, at least in part, explain the distribution of optical signal, further details of the actual spatio-temporal dynamics of the membrane potential response should be examined elsewhere.

Our simulations indicate that the population nature of the optical signal may be useful in detecting the synchronicity of action potentials in a neuronal circuit, which is often important for representing information in the brain (Mann et al., 2005b; Schaefer et al., 2006). It would also be useful to visualize how inhibitory inputs actually act within the neuronal circuit during memory formation and retrieval (Buzsáki, 2002). Once optical signals are confirmed to be accurate representations of population signals, then because of its simplicity, optical recording should be promoted as a useful method for evaluating neuronal information processing based on a balance of excitatory and inhibitory inputs to neurons (Liu, 2004).

GABAergic transmission in the CNS has great importance in terms of the development of pharmacological targets for treating various mental disorders. A robust recording method like optical recording to monitor the inhibitory activity of neuronal tissue should provide one solution to the growing demands for quick and comprehensive assay methods for physiological responses.

References

Aihara, T., Kobayashi, Y., Tsukada, M., 2005. Spatiotemporal visualization of long-term potentiation and depression in the hippocampal CA1 area. Hippocampus 15, 68–78.

Alger, B.E., Nicoll, R.A., 1982a. Pharmacological evidence for two kinds of GABA receptor on rat hippocampal pyramidal cells studied in vitro. J. Physiol. (Lond.) 328, 125–141.

Alger, B.E., Nicoll, R.A., 1982b. Feed-forward dendritic inhibition in rat hippocampal pyramidal cells studied in vitro. J. Physiol. (Lond.) 328, 105–123.

Andersen, P., Eccles, J.C., Loyning, Y., 1963. Recurrent inhibition in the hippocampus with identification of the inhibitory cell and its synapses. Nature 198, 540–542.
Andersen, P., Eccles, J.C., Loyning, Y., 1964. Pathway of postsynaptic inhibition in the hippocampus. J. Neurophysiol. 27, 608–619.
Andersen, P., Gross, G.N., Lomo, T., Sveen, O., 1969a. Participation of inhibitory and excitatory interneurones in the control of hippocampal cortical output. UCLA Forum Med. Sci. 11, 415–465.
Andersen, P., Bliss, T.V., Lomo, T., Olsen, L.I., Skrede, K.K., 1969b. Lamellar organization of hippocampal excitatory pathways. Acta Physiol. Scand. 76, 4A–5A.
Andersen, P., Dingledine, R., Gjerstad, L., Langmoen, I.A., Laursen, A.M., 1980. Two different responses of hippocampal pyramidal cells to application of gamma-amino butyric acid. J. Physiol. (Lond.) 305, 279–296.
Antic, S., Zecevic, D., 1995. Optical signals from neurons with internally applied voltage-sensitive dyes. J. Neurosci. 15, 1392–1405.
Antic, S.D., 2003. Action potentials in basal and oblique dendrites of rat neocortical pyramidal neurons. J. Physiol. 550, 35–50.
Barish, M.E., Ichikawa, M., Tominaga, T., Matsumoto, G., Iijima, T., 1996. Enhanced fast synaptic transmission and a delayed depolarization induced by transient potassium current blockade in rat hippocampal slice as studied by optical recording. J. Neurosci. 16, 5672–5687.
Brown, T.H., Johnston, D., 1983. Voltage-clamp analysis of mossy fiber synaptic input to hippocampal neurons. J. Neurophysiol. 50, 487–507.
Buhl, E.H., Han, Z.S., Lorinczi, Z., Stezhka, V.V., Karnup, S.V., Somogyi, P., 1994. Physiological properties of anatomically identified axo-axonic cells in the rat hippocampus. J. Neurophysiol. 71, 1289–1307.
Buzsaki, G., 1984. Feed-forward inhibition in the hippocampal formation. Prog. Neurobiol. 22, 131–153.
Buzsáki, G., 2002. Theta oscillations in the hippocampus. Neuron 33, 325–340.
Chang, P.Y., Jackson, M.B., 2003. Interpretation and optimization of absorbance and fluorescence signals from voltage-sensitive dyes. J. Membr. Biol. 196, 105–116.
Chang, P.Y., Jackson, M.B., 2006. Heterogeneous spatial patterns of long-term potentiation in rat hippocampal slices. J. Physiol. 576, 427–443.
Cobb, S.R., Halasy, K., Vida, I., Nyiri, G., Tamas, G., Buhl, E.H., Somogyi, P., 1997. Synaptic effects of identified interneurons innervating both interneurons and pyramidal cells in the rat hippocampus. Neuroscience 79, 629–648.
Cohen, L.B., Salzberg, B.M., Davila, H.V., Ross, W.N., Landowne, D., Waggoner, A.S., Wang, C.H., 1974. Changes in axon fluorescence during activity: molecular probes of membrane potential. J. Membr. Biol. 19, 1–36.
Conti, F., Tasaki, I., 1970. Changes in extrinsic fluorescence in squid axons during voltage-clamp. Science 169, 1322–1324.
Davie, J.T., Kole, M.H., Letzkus, J.J., Rancz, E.A., Spruston, N., Stuart, G.J., Hausser, M., 2006. Dendritic patch-clamp recording. Nat. Protoc. 1, 1235–1247.
de Curtis, M., Takashima, I., Iijima, T., 1999. Optical recording of cortical activity after in vitro perfusion of cerebral arteries with a voltage-sensitive dye. Brain Res. 837, 314–319.
Dingledine, R., Langmoen, I.A., 1980. Conductance changes and inhibitory actions of hippocampal recurrent IPSPs. Brain Res. 185, 277–287.
Dingledine, R., Gjerstad, L., 1980. Reduced inhibition during epileptiform activity in the in vitro hippocampal slice. J. Physiol. 305, 297–313.
Freund, T.F., Buzsaki, G., 1996. Interneurons of the hippocampus. Hippocampus 6, 347–470.
Glickfeld, L.L., Scanziani, M., 2006. Distinct timing in the activity of cannabinoid-sensitive and cannabinoid-insensitive basket cells. Nat. Neurosci. 9, 807–815.
Golding, N.L., Spruston, N., 1998. Dendritic sodium spikes are variable triggers of axonal action potentials in hippocampal CA1 pyramidal neurons. Neuron 21, 1189–1200.
Griffith, W.H., Brown, T.H., Johnston, D., 1986. Voltage-clamp analysis of synaptic inhibition during long-term potentiation in hippocampus. J. Neurophysiol. 55, 767–775.
Grinvald, A., Manker, A., Segal, M., 1982. Visualization of the spread of electrical activity in rat hippocampal slices by voltage-sensitive optical probes. J. Physiol. 333, 269–291.
Hines, M.L., Carnevale, N.T., 1997. The NEURON simulation environment. Neural Comput. 9, 1179–1209.
Inoue, M., Hashimoto, Y., Kudo, Y., Miyakawa, H., 2001. Dendritic attenuation of synaptic potentials in the CA1 region of rat hippocampal slices detected with an optical method. Eur. J. Neurosci. 13, 1711–1721.
Johnston, D., Christie, B.R., Frick, A., Gray, R., Hoffman, D.A., Schexnayder, L.K., Watanabe, S., Yuan, L.L., 2003. Active dendrites, potassium channels and synaptic plasticity. Philos. Trans. R. Soc. Lond. B Biol. Sci. 358, 667–674.
Kajiwara, R., Wouterlood, F.G., Sah, A., Boekel, A.J., Baks-te Bulte, L.T., Witter, M.P., 2008. Convergence of entorhinal and CA3 inputs onto pyramidal neurons and interneurons in hippocampal area CA1—an anatomical study in the rat. Hippocampus 18, 266–280.
Kandel, E., Spencer, W., Brinley, F.J., 1961. Electrophysiology of hippocampal neurons. I. Sequential invasion and synaptic organization. J. Neurophysiol. 24, 225–242.
Karnup, S., Stelzer, A., 1999. Temporal overlap of excitatory and inhibitory afferent input in guinea-pig CA1 pyramidal cells. J. Physiol. 516 (Pt 2), 485–504.
Kawamura, Y., Manita, S., Nakamura, T., Inoue, M., Kudo, Y., Miyakawa, H., 2004. Glutamate release increases during mossy-CA3 LTP but not during Schaffer-CA1 LTP. Eur. J. Neurosci. 19, 1591–1600.
Kojima, S., Nakamura, T., Nidaira, T., Nakamura, K., Ooashi, N., Ito, E., Watase, K., Tanaka, K., Wada, K., Kudo, Y., Miyakawa, H., 1999. Optical detection of synaptically induced glutamate transport in hippocampal slices. J. Neurosci. 19, 2580–2588.
Lacaille, J.C., Schwartzkroin, P.A., 1988a. Stratum lacunosum-moleculare interneurons of hippocampal CA1 region II. Intrasomatic and intradendritic recordings of local circuit synaptic interactions. J. Neurosci. 8, 1411–1424.
Lacaille, J.C., Schwartzkroin, P.A., 1988b. Stratum lacunosum-moleculare interneurons of hippocampal CA1 region. I. Intracellular response characteristics, synaptic responses, and morphology. J. Neurosci. 8, 1400–1410.
Liu, G., 2004. Local structural balance and functional interaction of excitatory and inhibitory synapses in hippocampal dendrites. Nat. Neurosci. 7, 373–379.
Magee, J.C., Johnston, D., 1995. Synaptic activation of voltage-gated channels in the dendrites of hippocampal pyramidal neurons. Science 268, 301–304.
Mann, E.O., Paulsen, O., 2005. Mechanisms underlying gamma ('40 Hz') network oscillations in the hippocampus—a mini-review. Prog. Biophys. Mol. Biol. 87, 67–76.
Mann, E.O., Paulsen, O., 2006. Keeping inhibition timely. Neuron 49, 8–9.
Mann, E.O., Tominaga, T., Ichikawa, M., Greenfield, S.A., 2005a. Cholinergic modulation of the spatiotemporal pattern of hippocampal activity in vitro. Neuropharmacology 48, 118–133.
Mann, E.O., Suckling, J.M., Hajos, N., Greenfield, S.A., Paulsen, O., 2005b. Perisomatic feedback inhibition underlies cholinergically induced fast network oscillations in the rat hippocampus in vitro. Neuron 45, 105–117.
Megias, M., Emri, Z., Freund, T.F., Gulyas, A.I., 2001. Total number and distribution of inhibitory and excitatory synapses on hippocampal CA1 pyramidal cells. Neuroscience 102, 527–540.
Migliore, M., 2003. On the integration of subthreshold inputs from Perforant Path and Schaffer Collaterals in hippocampal CA1 pyramidal neurons. J. Comput. Neurosci. 14, 185–192.
Migliore, M., Hoffman, D.A., Magee, J.C., Johnston, D., 1999. Role of an A-type K+ conductance in the back-propagation of action potentials in the dendrites of hippocampal pyramidal neurons. J. Comput. Neurosci. 7, 5–15.
Mochida, H., Sato, K., Sasaki, S., Yazawa, I., Kamino, K., Momose-Sato, Y., 2001. Effects of anisomycin on LTP in the hippocampal CA1: long-term analysis using optical recording. Neuroreport 12, 987–991.
Nevian, T., Larkum, M.E., Polsky, A., Schiller, J., 2007. Properties of basal dendrites of layer 5 pyramidal neurons: a direct patch-clamp recording study. Nat. Neurosci. 10, 206–214.
Pouille, F., Scanziani, M., 2001. Enforcement of temporal fidelity in pyramidal cells by somatic feed-forward inhibition. Science 293, 1159–1163.
Pouille, F., Scanziani, M., 2004. Routing of spike series by dynamic circuits in the hippocampus. Nature 429, 717–723.
Remondes, M., Schuman, E.M., 2002. Direct cortical input modulates plasticity and spiking in CA1 pyramidal neurons. Nature 416, 736–740.
Remondes, M., Schuman, E.M., 2003. Molecular mechanisms contributing to long-lasting synaptic plasticity at the temporoammonic-CA1 synapse. Learn. Mem. 10, 247–252.
Ross, W.N., Salzberg, B.M., Cohen, L.B., Grinvald, A., Davila, H.V., Waggoner, A.S., Wang, C.H., 1977. Changes in absorption, fluorescence, dichroism, and Birefringence in stained giant axons: optical measurement of membrane potential. J. Membr. Biol. 33, 141–183.
Sayer, R.J., Redman, S.J., Andersen, P., 1989. Amplitude fluctuations in small EPSPs recorded from CA1 pyramidal cells in the guinea pig hippocampal slice. J. Neurosci. 9, 840–850.
Schaefer, A.T., Angelo, K., Spors, H., Margrie, T.W., 2006. Neuronal oscillations enhance stimulus discrimination by ensuring action potential precision. PLoS Biol. 4, e163.
Sjostrom, P.J., Rancz, E.A., Roth, A., Hausser, M., 2008. Dendritic excitability and synaptic plasticity. Physiol. Rev. 88, 769–840.
Stuart, G.J., Dodt, H.U., Sakmann, B., 1993. Patch-clamp recordings from the soma and dendrites of neurons in brain slices using infrared video microscopy. Pflugers Arch. 423, 511–518.
Tominaga, T., Tominaga, Y., Ichikawa, M., 2001. Simultaneous multi-site recordings of neural activity with an inline multi-electrode array and optical measurement in rat hippocampal slices. Pflugers Arch. 443, 317–322.
Tominaga, T., Tominaga, Y., Ichikawa, M., 2002. Optical imaging of long-lasting depolarization on burst stimulation in area CA1 of rat hippocampal slices. J. Neurophysiol. 88, 1523–1532.
Tominaga, T., Tominaga, Y., Yamada, H., Matsumoto, G., Ichikawa, M., 2000. Quantification of optical signals with electrophysiological signals in neural activities of Di-4-ANEPPS stained rat hippocampal slices. J. Neurosci. Methods 102, 11–23.
Tominaga, Y., Ichikawa, M., Tominaga, T., 2003. Visualization of steady membrane potential change in area CA1 of rat hippocampal slices with voltage sensitive dye optical imaging. In: Society for Neuroscience. New Orleans, .
Turner, D.A., 1988. Waveform and amplitude characteristics of evoked responses to dendritic stimulation of CA1 guinea-pig pyramidal cells. J. Physiol. 395, 419–439.
Turner, D.A., 1990. Feed-forward inhibitory potentials and excitatory interactions in guinea-pig hippocampal pyramidal cells. J. Physiol. 422, 333–350.
Verheugen, J.A., Fricker, D., Miles, R., 1999. Noninvasive measurements of the membrane potential and GABAergic action in hippocampal interneurons. J. Neurosci. 19, 2546–2555.